

Global MS/MS Epigenetic Analysis of DNA Damage Response

1

2 **Global Epigenetic Analysis Reveals H3K27 Methylation as a Mediator of Double** 3 **Strand Break Repair**

4

5 Julian Lutze¹, Donald Wolfgeher² & Stephen J. Kron^{1,2}

6

7 1: Committee on Cancer Biology, The University of Chicago, IL, USA

8 2: Department of Molecular Genetics and Cell Biology, The University of Chicago, IL,
9 USA

10

11 Running Title: Global MS/MS Epigenetic Analysis of DNA Damage Response

12

13 Abbreviations: AMT, Accurate Mass and time; ATM, Ataxia telangiectasia mutated;
14 ATR, Ataxia telangiectasia and Rad3 related; DDR, DNA Damage Response; DSB
15 Double Strand Break; DNA-PKcs, DNA-dependent Protein Kinase; EHMP, Epiproteomic
16 Histone Modification Panel; EZH2, Enhancer of Zest Homologue 2; FRET, Förster
17 Resonance Energy Transfer; γH2AX, gamma H2AX is the phosphorylated form of
18 H2AX; HR, Homologous Recombination; IR, Ionizing Radiation; IRIF, Ionizing Radiation
19 Induced Foci; NHEJ, Non-homologous End Joining; MRM, Multiple Reaction Monitoring;
20 PARP, Poly ADP-ribose Polymerase; PIKK, Phosphatidylinositol 3-kinase-related

Global MS/MS Epigenetic Analysis of DNA Damage Response

- 21 kinases; PIR, Post-IR; Pol II, RNA Polymerase II; PRC2, Polycomb Repressive
- 22 Complex 2; PTM, Post Translational Modification
- 23

Global MS/MS Epigenetic Analysis of DNA Damage Response

Abstract

The majority of cancer patients is treated with ionizing radiation (IR), a relatively safe and effective treatment considered to target tumors by inducing DNA double strand breaks (DSBs). Despite clinical interest in increasing the efficacy of IR by preventing successful DSB repair, few effective radio-adjuvant therapies exist. Extensive literature suggests that chromatin modifiers play a role in the DSB repair and thus may represent a novel class of radiosensitizers. Indeed, chromatin has both local and global impacts on DSB formation, recognition of breaks, checkpoint signaling, recruitment of repair factors, and timely DSB resolution, suggesting that epigenetic deregulation in cancer may impact the efficacy of radiotherapy. Here, using tandem mass spectrometry proteomics to analyze global patterns of histone modification in MCF7 breast cancer cells following IR exposure, we find significant and long-lasting changes to the epigenome. Our results confirm that H3K27 trimethylation (H3K27me3), best known for mediating gene repression and regulating cell fate, increases after IR. H3K27me3 changes rapidly, accumulating at sites of DNA damage. Inhibitors of the Polycomb related complex subunit and H3K27 methyltransferase EZH2 confirm that H3K27me3 is necessary for DNA damage recognition and cell survival after IR. These studies provide an argument for evaluating EZH2 as a radiosensitization target and H3K27me3 as a marker for radiation response in cancer. Proteomic data are available via ProteomeXchange with identifier PXD019388.

Global MS/MS Epigenetic Analysis of DNA Damage Response

Introduction

Ionizing radiation (IR) remains one of the most widely utilized treatments for cancer, irrespective of organ site or disease stage^{1,2}. Modern clinical irradiators can deliver ablative IR doses precisely to the tumor volume while sparing adjacent normal tissue. Even so, radiotherapy is typically ineffective on its own^{3,4} and overcoming resistance often depends on combinations with cytotoxic chemotherapy, which incur greater toxicity⁵⁻⁷. An attractive alternative is to identify agents that can enhance local effects of IR on tumor cells but have minimal impacts on unirradiated, normal tissue^{8,9}. Although promising candidate radiosensitizers have been identified, failures in translation to the clinic highlight gaps in understanding of radiation response and mechanisms underpinning radiosensitization targets¹⁰⁻¹². Here, we add to a growing body of literature which establishes chromatin and its constituent histones as key mediators of DNA damage response (DDR) after IR¹³. We further show that modulation of readers and writers of histone post-translational modifications is sufficient to disrupt the cellular response to IR, thereby uncovering additional radiosensitization targets.

Most radiation damage is to DNA bases or single strands, but when IR-induced free radicals react with both strands of chromosomal DNA in proximity, the result can be a double strand break (DSB). DSBs are acutely lethal to cells and are considered the key mediator of radiation's therapeutic effects; failure of DSB repair can lead to chromosomal instability or aneuploidy¹⁴. However, as direct reporters of DSB intracellular location are not yet available, the extent of DSBs is commonly assayed via recruitment of proxy proteins or histone modifications. Prior to any repair, DNA damage must be detected, and break loci marked to direct recruitment of signaling and repair

Global MS/MS Epigenetic Analysis of DNA Damage Response

factors. The Phosphatidylinositol 3-kinase-related kinases (PIKKs) ataxia telangiectasia mutated (ATM), Ataxia telangiectasia and Rad3 related (ATR) and DNA-dependent protein kinase (DNA-PKcs) are early responders recruited to DSB loci to mark nearby histone H2AX by phosphorylating Ser139 to form γ H2AX^{15,16}. γ H2AX forms punctate intracellular foci termed IR induced foci (IRIF) which are thought to demarcate repair loci^{17,18}. In parallel, poly-ADP ribose polymerase 1 (PARP1) and other PARPs bind proximal to DNA breaks and subsequently PAR-ylate histones and other local substrates, perhaps to affect chromatin decondensation^{19–21}. Following break recognition, DSB rejoining is classically described as a choice between two pathways, non-homologous end joining (NHEJ) and homologous recombination (HR)^{22,23}. Together these pathways collaborate to restore DNA integrity and limit chromosomal instability^{24–27}.

It is widely recognized that chromatin and histone post-translational modifications (PTMs) beyond H2AX phosphorylation impinge upon recognition of DSBs and direct deposition of γ H2AX prior to break repair. A range of epigenetic reader and writer enzymes, previously established as transcriptional regulators, have also been implicated in DSB sensing, signaling and repair^{28–35}. However, many of these studies are subject to the caveat that DSB formation after IR is dramatically affected by chromatin state. Chromosomal DNA packaged into heterochromatin is intrinsically radiation-resistant compared to actively transcribed DNA^{36–39}. Experiments examining epigenetic regulators in DNA damage response typically lack the temporal resolution to distinguish effects on DSB formation from detection or repair. Further, without a direct

Global MS/MS Epigenetic Analysis of DNA Damage Response

reporter of DSBs, deconvoluting effects of histone modifiers on IRIF formation or resolution is challenging.

An illustrative example is enhancer of zeste homologue 2 (EZH2), a catalytic subunit of the polycomb repressive complex 2 (PRC2). EZH2 modifies histone H3 to form H3K27me₃, a repressive histone mark associated with heterochromatin. PRC2 plays a central role in development, gene silencing, and cell fate decisions via selective deposition of H3K27me₃ to assemble heterochromatin^{40–43}. As heterochromatin is intrinsically radioresistant, inhibiting EZH2 for one or more cell cycles may phenocopy radiosensitizers by increasing the yield of DSBs without affecting recruitment of DDR factors or recognition of damage. However, EZH2 and other PRC2 subunits also localize to DSBs^{44,45} where EZH2 may deposit H3K27me₃ on DSB-proximal nucleosomes⁴⁶. Blocking EZH2 activity immediately prior to irradiation can delay DSB repair, apparently by slowing NHEJ, though inhibiting EZH2 also leads to increased γH2AX levels 24 h after IR insult when NHEJ is no longer thought to participate in repair^{47–49}. EZH2 also methylates non-histone substrates and interacts with other DNA damage response factors, adding further complexity^{50–52}. Along with concerns about conflating local and global effects, the notion that a histone mark which mediates heterochromatin contributes to DSB repair is paradoxical as successful repair requires recruitment of several factors and access to DNA.

Development of radiosensitizers has heretofore focused on processes downstream of break recognition such as cell cycle disruption and cell fate. However, a focus on global signaling belies chromatin localized steps critical to DSB repair. The complexity of DSB repair across a varied epigenome coupled with imprecise

Global MS/MS Epigenetic Analysis of DNA Damage Response

measurements of DSB repair render radiosensitizer identification challenging. It is thought that small molecules targeting DSB detection by PIKKs or PARPs sensitize cell lines and tumor models to radiation by preventing DSB repair, but clinical translation has lagged^{53,54}. Further, inhibitors of epigenetic readers and writers appear to be attractive radiosensitization targets, but a fuller understanding of their mechanism of action is needed before they can be used clinically.

Toward identifying epigenetic marks that are modulated by DSBs, we used targeted proteomics to evaluate the dynamics of several dozen histone modifications in total chromatin following irradiation. Based on patterns of regulation, this broad survey pointed back to EZH2 as a critical regulator. Toward validating these findings, we confirmed a role for PRC2 in DSB recognition and showed that deregulation of H3K27 modification impacts cellular responses to IR.

Global MS/MS Epigenetic Analysis of DNA Damage Response

Experimental Procedures

Cell Culture

MCF7 cells were grown in DMEM medium supplemented with 10% fetal bovine serum (Atlanta) and 4mM L-Glutamine, in a humidified atmosphere of 5% CO₂ maintained at 37°C. All cells were originally obtained from the American Type Culture Collection (ATCC). The cells were tested for mycoplasma contamination and authenticated by short tandem repeat profile (IDEXX, BioResearch) prior to performing experiments. All experiments were performed within 3 to 10 passages after thawing cells.

Antibodies

Antibodies used for immunofluorescence in this study are as follows. γH2AX (mouse mAb, clone JBW301, Millipore Sigma) histone H3K27me3 (rabbit, mAb, clone C36B11, CST) histone H3 (mouse, mAb, clone 6.6.2, Millipore Sigma), RNA Polymerase 2 (rabbit polyclonal) R-Loop (Abcam, Rabbit mAb clone S9.6). Secondary antibodies are sheep anti-mouse, Alexa Fluor 488, goat anti-rabbit, Alexa Fluor 647 and Alexa Fluor 595, all sourced from Jackson ImmunoResearch.

Inhibitors and drug treatment

Small molecule probes used in this study were GSK126, an EZH2 inhibitor, and GSKJ4 HCL, a JMJD2/3 inhibitor (Selleck Chem) and veliparib, a PARP inhibitor (obtained from Abbvie). Inhibitor stocks were diluted to 10 mM in DMSO and added to cells for the indicated length of time. Unless otherwise noted, final concentrations used were as

Global MS/MS Epigenetic Analysis of DNA Damage Response

follows: GSK126, 20 μ M; GSKJ4, 10 μ M; Veliparib 10 μ M. DMSO was used at 1:1000 dilution for vehicle treatments.

DNA damage treatment

DNA damage was induced by exposure to a ^{60}Co γ -ray source. Cells were placed in an irradiator (MDS Nordion) and exposed to the indicated dose. Dosage rates varied between 10.5 and 9.1 cGy/s depending on the date of the experiment. Cells were allowed to recover in incubator for the indicated time. Non-irradiated (NIR) samples were mock irradiated.

Multiple Reaction Monitoring (MRM) analysis of histone PTMs

Initial histone PTM analysis was performed by the Northwestern University Proteomics Core. We used the Epiproteomic Histone Modification Panel B assay. The method, in brief, is as follows. Histones were extracted directly from flash frozen cell pellets with the addition of 5 volumes of 0.2 M H_2SO_4 for 1 h at room temperature (RT). Cellular debris was removed by centrifugation at 4,000 x g for 5 min and histones were precipitated from the supernatant with trichloroacetic acid (TCA) at a final concentration of 20% (v/v) for 1 h on ice. Precipitated histones were pelleted at 10,000 x g for 5 minutes, washed once with 0.1% HCl in acetone then twice with 100% acetone with centrifugation at 15,000 x g for 5 minutes. After the final acetone wash, histones were dried briefly and stored at -20 °C until derivatization. Histones were propionylated and digested according to Garcia et al. ⁵⁵, with the modification of a single round of

Global MS/MS Epigenetic Analysis of DNA Damage Response

propionylation for 1 h prior to and following digestion. Targeted MRM LC-MS/MS was performed on a TSQ Quantiva (Thermo Scientific) triple quadrupole mass spectrometer. This Histone PTM MRM panel B, assaying 95 modification states and their transitions, was developed and setup at the Northwestern Proteomics core and raw data analyzed in Skyline 2 according to published methods⁵⁶.

Histone PTM data analysis

Data obtained from the MRM analysis were provided as a rectangular matrix with each row representing a PTM and each column containing either the raw peak area (peptide intensity value) or the residue-normalized percentage of a given PTM in a given sample. tSNE analysis was performed in R with the RtNSE package on the residue-normalized data. Default settings were used, though the perplexity was set to 1 because of the low number of datapoints. For clustering of PTMs, raw peak area data were used. The package dtwclust was utilized to perform the DTW distance calculations to obtain more accurate relationships between time-series data. The number of clusters was set at 5 after manual inspection of the elbow plot generated by dtwclust and clustering was carried out via the partitioning around medoids (PAM) algorithm. A heatmap was created using the heatmap2 package in R with a Euclidean distance metric and a Ward D2 clustering algorithm. All plots were generated using ggplot2 implemented in base R or the tidyverse packages. All code used to generate the figures is available upon request.

Global MS/MS Epigenetic Analysis of DNA Damage Response

Histone sample preparation for LC-MS/MS

Briefly, 5×10^6 cells were harvested, and nuclei were isolated using NEB buffer (10 mM HEPES pH 7.9, 1 mM KCl, 1.5 mM $MgCl_2$, 1mM DTT). Histones were extracted from nuclei by treatment with 0.4 N H_2SO_4 (Sigma 258105-500mL) for 30 minutes at room temperature and then precipitated from the supernatant by dropwise addition of ice-cold trichloroacetic acid (Sigma T069-100mL). Precipitated protein was spun down and washed twice with very-cold acetone (Fisher A18-500). The pellet was then air dried and resuspended in ddH₂O. For each sample set, 20 μ g of protein (determined via Bradford assay), was loaded and run into a MOPS (Thermo, NuPage NP0001) buffered a 1D 12% gel plug (Thermo NP0341BOX) for 6 min at 200 V.

Gel sections were subjected to propionyl derivatization (at the protein level), Trypsin digestion, propionyl derivatization (at the peptide level), followed by C18 cleanup. For propionyl derivatization, propionic anhydride (Sigma 240311-50g) was mixed 1:3 with isopropanol (ACROS 42383-0040) pH 8.0 and reacted 37 °C for 15 minutes. Following protein derivatization treatment, gel sections were washed in dH₂O and de-stained using 100 mM NH_4HCO_3 (Sigma 285099) pH 7.5 in 50% acetonitrile (Fisher A998SK-4). A reduction step was performed by addition of 100 μ l 50 mM NH_4HCO_3 pH 7.5 and 10 μ l of 200 mM tris(2-carboxyethyl) phosphine HCl (Sigma C4706-2G) at 37 °C for 30 min. The proteins were alkylated by addition of 100 μ l of 50 mM iodoacetamide (Sigma RPN6320V) prepared fresh in 50 mM NH_4HCO_3 pH 7.5 buffer and allowed to react in the dark at 20 °C for 30 minutes. Gel sections were washed in water, then acetonitrile.

Global MS/MS Epigenetic Analysis of DNA Damage Response

Trypsin digestion was carried out overnight at 37 °C with 1:50-1:100 enzyme–protein ratio of sequencing grade-modified trypsin (Promega V5111) in 50 mM NH_4HCO_3 pH 7.5, and 20 mM CaCl_2 (Sigma C-1016). Peptides were extracted with 5% formic acid (Sigma F0507-1L), then 5% formic acid with 75% ACN, combined and vacuum dried. Post-digestion, peptides were derivatized with propionic anhydride:IPA 1:3 at 37 °C for 15 min and repeated for a total of two times. Peptides were then cleaned up with C18 spin columns (Thermo 89870). and sent to the Mayo Clinic Medical Genome Facility Proteomics Core for HPLC and LC-MS/MS data acquisition via Q-Exactive Orbitrap (Thermo).

LC-MS/MS and PTM analysis via EpiProfile and MaxQuant

Peptide samples were re-suspended in Burdick & Jackson HPLC-grade water containing 0.2% formic acid (Fluka 94318-50ML), 0.1% TFA (Pierce 28903), and 0.002% Zwittergent 3–16 (Calbiochem 14933-09-6), a sulfobetaine detergent that contributes the following distinct peaks at the end of chromatograms: MH^+ at 392, and in-source dimer $[2\text{ M} + \text{H}^+]$ at 783, and some minor impurities of Zwittergent 3-12 seen as MH^+ at 336. The peptide samples were loaded to a 0.25uL OptiPak trap (Optimize Technologies, Oregon City, OR) custom-packed with 5um Magic C18-AQ (Michrom BioResources, Inc., Auburn, CA). washed, then switched in-line with a nanoLC column ~34cm x 100um i.d. PicoFrit column (New Objective, Woburn, MA) self-packed with Agilent Poroshell 120S ES-C18, 2.7 um stationary phase. Column flow was 400 nl/min. Mobile phase A was water/acetonitrile/formic acid (98/2/0.2) and mobile phase B was acetonitrile/isopropanol/water/formic acid (80/10/10/0.2). Using a flow rate of 350 nl/min,

Global MS/MS Epigenetic Analysis of DNA Damage Response

a 90 min, 2-step LC gradient was run from 5% B to 50% B in 60 min, followed by 50%–95% B over the next 10 min, hold 10 min at 95% B, back to starting conditions and re-equilibrated.

Electrospray tandem mass spectrometry (LC-MS/MS) was performed at the Mayo Clinic Proteomics Core on a Thermo Q-Exactive Orbitrap mass spectrometer, using a 70,000 RP survey scan in profile mode, m/z 340–2000 Da, with lockmasses, followed by 20 MSMS HCD fragmentation scans at 17,500 resolution on doubly and triply charged precursors. Single charged ions were excluded, and ions selected for MS/MS were placed on an exclusion list for 60 seconds. An inclusion list (generated with in-house software) consisting of expected histone PTMs was used during the LC-MS/MS runs.

For EpiProfile analysis, sample *.raw files were extracted and peak picking performed using with pXtract version 2.0 to obtain their MS1 and MS2 files⁵⁷. These along with their *.raw files were analyzed in Matlab with the Epiprofile 2.0 script^{58,59}. In addition to the Epiprofile modifications detected, we wanted to probe for any additional common and unique modifications, thus sample *.raw files were also searched in Maxquant version 1.5.2.8 (peaks picked in MaxQuant) against a histone protein fasta database downloaded 10/15/2019 from Uniprot. The PTM search was done in multiple searches at 20ppm with 1% FDR filtering using a fixed modification of Carbamidomethyl (C), common variable modifications of Deamidation (NQ), Formyl (n-term) Oxidation (M), combined with the following additional PTMS {**Ac** Acetylation (K,S,T), **Ar** ADP ribosylation (R,E,S), **Bu** Butyrylation (K), **Cit** Citruillination (R), **Cr** Crontonylation (K), **Fo** Formylation (K), **Hib** 2-Hydroxyl-isobutyrylation (K), **Ma**

Global MS/MS Epigenetic Analysis of DNA Damage Response

Malonylation (K), **Me** Methylation (K,R), **Me2** Di-Methylation (K,R), **Me3** Tri-Methylation (K,R), **Og** O-glycacylation (S,T), **Oh** Hydroxylation (Y), **Ph** Phosphorylation (S,T,Y), **Pr** Propionylation (K), **Su** Succinylation (K), and **Ub** Ubiquitylation aka GlyGly (K)}.

Downstream PTM analysis was performed in Perseus version 1.6.7.0⁶⁰ and formatted in Perseus, Excel (Microsoft) or R. All code is available upon request. All mass spectrometry proteomics data have been deposited to the ProteomeXchange Consortium via the PRIDE partner repository with the dataset identifier PXD019388^{61,62}.

Immunofluorescence imaging and foci analysis

For all imaging, 2.5×10^4 MCF7 cells were seeded on round #1.5 cover glass in 24 well plates and incubated until 50-80% confluency was achieved. Irradiation and/or treatment with indicated inhibitors were performed *in situ*. For slide preparation, cells were fixed with 4% PFA in PBS for 10 minutes at the indicated time point, stained with 0.5 µg/mL DAPI, and mounted using ProLong Gold (Invitrogen). For immunofluorescence staining, cells were fixed as above, then permeabilized with 10% Triton-X 100 for 10 minutes. After blocking with 5% BSA (American Scientific) in PBS for 1 h, the indicated primary antibodies were added and coverslips were incubated overnight at 4°C. All antibodies were used at 1:1000 dilution. Following three 5 minute washes with 5% BSA in PBS supplemented with 0.1% TX-100 and 0.05% NP-40, fluorescent secondary antibodies (Jackson ImmunoResearch) were applied for 1 h at RT. Foci images were captured on an Olympus IX81 wide-field microscope with either a 40 X or 100 X oil-immersion objective and pseudo colored using ImageJ. Two or more

Global MS/MS Epigenetic Analysis of DNA Damage Response

replicates were performed for each experiment and greater than 50 cells were imaged per replicate.

Foci counting was performed with a custom ImageJ macro. Briefly, nuclei were thresholded and segmented and foci were counted within each nucleus via a thresholding and FindMaxima routine. Foci intensity analysis was performed by segmenting the foci as above and then measuring the MFI within each focus. Foci size was determined by auto-local thresholding of the γ H2AX channel followed by segmentation and measurement of segmented foci regions. All other image analysis was carried out in ImageJ via custom macros. All macros available upon request.

Incucyte analysis

For analysis of cellular growth kinetics, MCF7 cells were seeded at low density (10% confluency) in 12-well plates and then treated as indicated. Plates were incubated in the Incucyte S3 imaging system (Essen Biosciences) for 5 days and images were recorded every 4 h. Confluency was calculated automatically using Incucyte software by manually thresholding a random selection of images and applying these settings to the entire image-set. Data were then normalized to the confluency at time of treatment. Plots were generated in R.

Comet single cell electrophoresis assay

MCF7 cells were irradiated and/or drug-treated as indicated before collection via trypsin and embedding in low-melting agarose (Trevigen). Comet assay was performed with a

Global MS/MS Epigenetic Analysis of DNA Damage Response

Trevigen Comet Kit according to manufacturer's directions with the following modifications. Cells were electrophoresed at 23 V for 60 min and stained with SYBR Green rather than SYBR Gold. Imaging of comet slides was carried out on a wide-field microscope with a 10 X air objective. Images were analyzed using ImageJ plugin OpenComet⁶³.

SA-βGal assay

Cells were seeded at 3×10^4 cells per well in six-well plates and treated with inhibitors for 1 h prior to irradiation. Cells were allowed to recover in a humidified incubator for 3 days before fixation and staining. Images were captured on a Zeiss Axiovert 200M microscope with a 20x Plan-NeoFluar objective and Axiocam digital camera controlled by OpenLab software. Two or more replicates were performed, and representative images are shown.

Colocalization analysis

Colocalization between two channels was determined by in-house code written to implement Li's ICA method⁶⁴. Briefly, ROIs corresponding to individual nuclei were segmented and cropped and images were saved as intensity matrices. A custom R script was written to transform corresponding matrices into colocalization scores. Pixels were considered to be colocalized if the intensity in a given pixel was above the mean intensity for an image in both channels. We reported the fraction of pixels within a given nuclear ROI which were colocalized. This method is insensitive both to the amount of

Global MS/MS Epigenetic Analysis of DNA Damage Response

staining present in an image and also to variations in intensity between cells or regions of an image.

Ground State Depletion (GSD) superresolution imaging

For superresolution imaging, cells were seeded on coverslips and stained as above but not mounted. Coverslips were washed 5X with PBS to remove non-specifically bound fluorophores, inverted over depression slides containing 50 μ l of freshly prepared 300 mM MEA oxygen scavenging medium, sealed with a two-part, quick-curing epoxy, and cured 5 minutes in a 50° C oven. For imaging, we utilized a Leica GSD 3D imaging system equipped with a 160 X/1.43 NA, 0.07 mm WD objective; Suppressed Motion (SuMo) stage; PiFoc precision focusing control system; blue (488 nm), green (532 nm) and red (642 nm) excitation lasers; fluorescein, rhodamine and far-red emission filters and an iXon Ultra EMCCD camera. Slides were then imaged using standard GSD imaging protocols with at least 10,000 frames captured per channel per image. GSD data analysis and processing were carried out with a series of in-house ImageJ macros. Identification of emission events was performed via ImageJ plugin ThunderSTORM⁶⁵. Final images were then pseudo colored and compiled in ImageJ. Superresolution imaging macros are available upon request.

GSD Fluorescence Resonance Energy Transfer (FRET) imaging

We labeled target proteins or PTMs with primary antibodies as indicated and utilized fluorescent secondary antibodies to introduce either a donor fluorophore (AF 594) or an

Global MS/MS Epigenetic Analysis of DNA Damage Response

acceptor fluorophore (AF 647), hereafter referred to as donor (DNR) and acceptor (ACC) respectively. First, both DNR and ACC were imaged at their respective excitation maxima to obtain an image of DNR and ACC location. Following high laser power exposure for 60s, both DNR and ACC were reimaged at their respective excitation maxima. The second ACC image displayed negligible signal indicating efficient bleaching on ACC fluorophores. Before ACC bleach, DNR energy was transferred to the ACC proportionately to the distance between DNR and ACC molecules. Bleached ACC fluorophores can no longer accept DNR energy, and all DNR energy is thus observed when exciting DNR fluorophores at DNR excitation maxima. Any increase in the DNR emission after ACC bleach is thus indicative of FRET and proportionate to the distance between ACC and DNR molecules. To obtain a FRET image, the DNR image before ACC bleach is subtracted from the DNR image after ACC bleach. The resultant image intensity is proportional to FRET between ACC and DNR. GSD-FRET reports both the location and the degree of FRET interactions between two labeled antigens. GSD-FRET imaging was carried out in the sequence described above. Images were pseudo-colored and manipulated in ImageJ.

Experimental Design and Statistical Rationale

For EMHP analysis, samples were analyzed in technical triplicate (n=3). For EpiProfile validation, biological triplicate samples were also collected (n=3). Number of replicates was selected based on standard proteomic experimental design. For EHMP analysis, peptides were selected in accordance with established protocols. For EpiProfile and MaxQuant analysis, data was generated with LC-MS/MS gradients compatible with

Global MS/MS Epigenetic Analysis of DNA Damage Response

EpiProfile, and ions were selected for MS/MS based on the Top20 most abundant peaks or if it appeared on an inclusion list consisting of common histone PTM proteolytic peptides' expected ion masses. Inclusion list ions were generated via in-house software selecting for (Ac, Me1-3, Ph or Ub PTMs across major histone isoforms). Peptides were selected using the EpiProfiler software or MaxQuant software according to default parameters. We performed non- controls for all experiments and data was collected in a time-course manner. Samples were not processed in a blinded fashion, though the order in which samples were processed was designed to minimize sample carryover and our protocol includes a blank injection between runs to mitigate column carryover. For EpiProfiler and MaxQuant analysis, raw files were searched at 1% FDR. A MaxQuant peptide cutoff score of 40 was also used for PTM peptide analysis. All statistical analysis was performed as indicated. Test were carried out in R using the ggpubr package. In general, a Wilcox Ranked-Sum Test was used to compare two samples. Kruskal-Wallis tests were used for analyses of more than two groups. For EpiProfile analysis, a Friedman test was performed in Prism (GraphPad). For all plots, significance values are as follows: ns $p > 0.05$; * $p < 0.05$; ** $p < 0.01$; *** $p < 0.001$; **** $p < 0.0001$. Box plots show first and third quartiles of the data as well as the median. In scenarios where multiple testing was considered, p-values were transformed into FDR q-values by the qvalues package in R (Storey method). All plots were generated in R using the ggplot, cowplot and ggpubr packages. Boxplots show the median, 1st and 3rd quartiles with whiskers extending to 1.5*IQR. All software versioning is described in Methods. All R code, for data generation, analysis, and plotting is available upon request.

Global MS/MS Epigenetic Analysis of DNA Damage Response

Results

Ionizing radiation induces widespread and long-lasting alterations to histone post-translational modifications

Targeted analyses probing one or a few histone post-translational modifications (PTMs) at a time have revealed a limited set of modifications that regulate the DNA damage response (DDR)^{66–68}. However, this work has not examined modifications beyond well-characterized epigenetic marks such as Ac, Me, Ph, and Ub, despite the rapidly growing list of dynamic histone modifications^{69,70}. Methods for proteomic analysis of global histone PTMs are now well established and provide broad coverage of most individual and many combinatorial histone modifications^{58,59}. Such methods have yet to be fully utilized to track epigenetic changes following genotoxic stress.

Toward surveying a broad range of epigenetic marks, we initially applied a multiple reaction monitoring (MRM)-based targeted quantitative triple-quadrupole mass spectrometry assay, the Epiproteomic Histone Modification Panel (EHMP, Northwestern Proteomics), to analyze multiple histone PTMs over a time course following irradiation of MCF7 breast carcinoma cells using a ⁶⁰Co source. ⁶⁰Co γ rays induce a wide range of DNA lesions, including a high fraction of complex DSBs which are characterized by multiple chemical changes that preclude rapid end-joining⁷¹. To sample a time-course spanning DSB formation to the anticipated completion of most repair⁷², MCF7 cells were irradiated with 6 Gy, returned to culture, and samples were collected at 1, 4, 24 and 48 h post IR (PIR). Acid-extracted histones from control and irradiated cells were subjected

Global MS/MS Epigenetic Analysis of DNA Damage Response

to the MRM histone PTM survey to measure modifications at a per-residue level. For residues which could be in any one of several modification states such as H3K9 (which may be unmodified, acetyl, mono-, di- or tri-methylated) analysis indicated the fraction of residues in each state. Thereby, 92 histone modifications were evaluated on 30 histone residues for each sample (Supplementary Table 1).

To assess overall changes in PTMs over the time course, the data for three technical replicates for each time point were examined by t-distributed stochastic neighbor embedding (tSNE) (Fig. 1a). Each time point after 6 Gy was distinct from the unirradiated (NIR) control. The 1 h and 4 h PIR samples clustered together and 24 h and 48 h PIR samples formed a separate cluster suggesting IR produces separable short and long-term changes to the epigenome. As a complementary approach, we applied hierarchical clustering (Fig. 1b), yielding relationships between the samples. The samples again fell into distinct groups corresponding to short-term and long-term changes. The shared patterns of PTM dynamics revealed by clustering were analyzed further by dynamic-time warping (DTW) analysis to extract temporally distinct modification trajectories (Fig. 1c). After clustering, five trajectories emerged from the data (Supplementary Table 2). Mapping the cluster centroids of each trajectory indicated a range of histone modification dynamics in response to DNA damage. In particular, Cluster 2 included many of the PTMs that increased sharply by 1 h PIR, including H3K9 methylation, H3K27 methylation, as well as H4 acetylation, known to mediate 53BP1 recruitment⁷³.

Toward identifying specific PTMs involved in the DNA damage response, we examined which modifications were significantly changed over the time course. Of the

Global MS/MS Epigenetic Analysis of DNA Damage Response

92 PTMs evaluated, 78 displayed significant changes at one or more timepoints after correcting for multiple testing (5% FDR; Kruskal-Wallis test) (Supplementary Table 3). Pointing to pathways that may mediate early events such as DNA damage recognition and signaling, 58 PTMs were significantly altered at 1 h PIR compared to non-irradiated cells after correcting for multiple testing (5% FDR; Wilcox Ranked-Sum Test, Fig. 1d) and 51 were both significantly higher at 1 h PIR and dynamic across the time course. This group included several PTMs previously linked to DSB repair including H3K79 methylation, catalyzed by Dot1L, and H4 methylation at K8, K12, K16 or K20, which mediate 53BP1 binding and NHEJ repair (Supplementary Fig 1)^{73,74}. Further validating this approach, our analysis identified H3K27 trimethylation ($q=0.031$, Kruskal-Wallis; $FC=1.153$, $q=0.0078$, Wilcox) as significantly increased 1 h PIR. As noted above, H3K27 trimethylation has been linked to DNA damage response and NHEJ^{45,48}, but mechanisms remain poorly defined.

An accurate mass and time approach confirms global epigenetic changes after irradiation

As a complementary approach, we performed an independent time-course analysis of chromatin modifications after irradiation using label-free, conventional LC-MS/MS and data analysis with EpiProfile 2.0⁵⁸, an accurate mass and time (AMT) strategy to quantify over 200 histone marks (Ac, Me1, Me2, Me3, and Ph). Following the EpiProfile protocol, histones from irradiated MCF7 cells were enriched by acidic extraction and then propionyl derivatized before and after trypsin digestion. The resulting peptides were subjected to Orbitrap LC-MS/MS in biological triplicate then examined with

Global MS/MS Epigenetic Analysis of DNA Damage Response

EpiProfile, manually validating spectra for PTM sites of interest. This analysis detected 204 PTM combinations reducing down to 45 single PTMs and found dynamic changes in 38 PTMs during the time course (Supplementary Table 4).

Focusing on modifications of histone H3 isoforms, we observed significant changes (Kruskal-Wallis, $p < 0.05$) across several residues including H3K27 and H3K36 (Supplementary Fig 2). We then plotted fold changes for PTMs on H3 residues at each of the four timepoints compared to unirradiated cells. The resulting heatmap revealed kinetically distinct patterns of dynamic modification for specific residues and PTMs including an increase in H3K27 and H3K36 methylation (Fig. 2a). Plotting relative PTM changes as compared to an unirradiated control, grouped by modification type, revealed a significant trend toward increased acetylation and conversion of mono-methylation to di- and tri-methylation, particularly during the first 24 h PIR (Fig. 2b). While effects of histone modifications are residue-specific, a global reduction in acetylation and an increase in methylation may suggest chromatin compaction or gene repression following IR. Next, we separated the H3K27 modification data by H3 isoform. This analysis revealed that H3.3 experiences the bulk of the observed reduction in K27 di-methylation as well as the increase in K27 tri-methylation (Fig. 2c-d). The MRM method was not powered to detect isoform level changes in H3, illustrating the added analytical power of EpiProfiler. H3.3 is enriched in euchromatin; thus, a potential role for increased H3K27me3, a PTM linked to transcriptional silencing, may be to suppress conflict between transcription and repair⁷⁵.

Comparing the DDA EpiProfile method to the MRM EHMP panel, and not accounting for unmodified peptides, EpiProfile detects a total of 161 PTMs and EHMP

Global MS/MS Epigenetic Analysis of DNA Damage Response

detects 63 PTMs, with 55 PTMs shared between the two methods. Considering only common PTMs, EpiProfile displayed an inter-replicate R^2 of 0.92 and EHMP an inter-replicate an R^2 of 0.99 after linear regression analysis. Nonetheless, comparing the two methods yields an R^2 of only 0.17 (Supplementary Fig 3), likely reflecting distinct biases between the two assays that affect sensitivity toward different PTMs.

Untargeted analysis reveals additional dynamic histone PTMs during the DNA damage response

Recent work has expanded the universe of histone modifications of importance beyond acetylation, methylation, phosphorylation and ubiquitinylation with the discovery of novel modifications including new PTMs such as Crononylation (Cr), Acetylations, O-GlcNAcylation (Og), Propionylation (Pr), Butyrylation (Bu), and ADP ribosylation (Ar)⁷⁰. To extend the analysis beyond the sites identified by EHMP or EpiProfile, the *.RAW data files obtained from QE-Orbitrap LC-MS/MS of the acid extracted and propionylated histone peptides were searched with MaxQuant to detect additional dynamic histone PTMs. We queried the EpiProfile data files for 17 additional PTMs: Ac, Ar, Bu, Cit, Cr, Fo, Hib, Ma, Me1, Me2, Me3, Og, OH, Ph, Pr, Su, Ub. PTMs were split into groups of 3-4 modifications to balance CPU load, search time, and data search space. This analysis detected 3076 total modifications across 5 time-points. (Supplementary Table 5, 6). Summary counts for unique PTMs were as follows, Ac: 516, Ar: 1, Bu: 236, Cit: 28, Cr: 132, Fo: ND, Hib: 64, Ma: 35, Me1: 531, Me2: 95, Me3: 171, Og: 39, OH: ND, Ph: 38, Pr: 956, Su: 28, Ub: 206). The ability to incorporate additional searches on EpiProfile data is an additional advantage over MRM methods such as EHMP. We acknowledge

Global MS/MS Epigenetic Analysis of DNA Damage Response

the ability to eventually add these new modifications to the EpiProfile MS based software as a custom search or potential version release. Although novel PTMs warrant further study, they remain challenging to assay experientially as readers and writers are unknown. Thus, we focused on the well characterized modification H3K27me3 which was highlighted by both EHMP and EpiProfile analyses above.

Inhibition of K3K27 methylation attenuates DSB recognition and repair

H3K27 trimethylation, mediated by the PRC2 catalytic subunit EZH2, is associated with transcriptional repression, heterochromatin formation and maintenance,^{76,77} and is also implicated in DSB detection and NHEJ repair^{44,78}. Demethylation by the jumonji-domain demethylases JMJD2 (KDM4A) and JMJD3 (KDM6B) opposes EZH2 activity^{79,80}. Toward establishing functional significance of H3K27 methylation in DSB recognition and repair, we acutely exposed MCF7 cells to EZH2 and/or JMJD2/3 inhibitors at tenfold over IC₅₀ to ablate enzyme activity prior to irradiation (Fig. 3a). As a control, we inhibited PARP1 with the non-trapping inhibitor veliparib⁸¹, known to delay DSB repair. Expected effects of each inhibitor on H3K27 methylation were confirmed by immunostaining with an anti-H3K27me3 antibody (Fig. S4a).

MCF7 cells were treated with the EZH2 inhibitor GSK126 (20 μ M) alone or in combination with the JMJD2/3 inhibitor GSKJ4 (10 μ M) for the indicated length of time, exposed to 6 Gy of IR, and allowed to recover for 1 h before being fixed and immunostained for γ H2AX 1 h PIR. Acute treatment with the inhibitors, alone or in combination, significantly decreased γ H2AX foci number after radiation (Fig. 3b). Additionally, we observed a significant reduction in fluorescence intensity of γ H2AX foci

Global MS/MS Epigenetic Analysis of DNA Damage Response

in cells treated with GSK126 and/or GSKJ4, suggesting that dysregulation of H3K27 methylation limits local H2AX phosphorylation (Fig. 3c). Conversely, treatment with the PARP inhibitor veliparib (10 μ M) somewhat increased γ H2AX foci number and intensity (Fig. 3b, c). The short interval between drug treatment and irradiation precludes effects dependent on gene repression or chromatin condensation and instead suggests that H3K27 methylation may be necessary for break recognition, as previously described⁷⁸ and that methylation acts upstream of H2AX phosphorylation.

To assess effects on radiation sensitivity, cells were treated with GSK126 alone or in combination with GSKJ4 for 1 h and irradiated with 6 Gy. The media was then replaced to relieve epigenetic inhibition, and cell growth was followed for 5 days by time-lapse imaging in an IncuCyte imaging incubator system. Here, the two drugs yielded different phenotypes: treating cells with the JMJD2/3 inhibitor completely blocked proliferation, while the EZH2 inhibitor attenuated recovery from IR (Fig. S4b). Single cell electrophoresis (comet) assay was performed to assess DSB repair independently from γ H2AX foci resolution. At 1 h PIR, we observed an increase in unrepaired DSBs following GSK126 treatment (Fig. 3d). These breaks persisted 24 h PIR, indicating that EZH2 inhibition leads to unrecognized or irreparable damage and loss of genomic stability. Examining the IncuCyte data, we observed both a decrease in proliferation and cell death following GSK126 treatment, likely a consequence of unrepaired DSBs (Fig. S4c). Toward establishing a mechanism by which short-term GSK126 treatment attenuates DDR repair, we examined transcription at DSB loci. In order to prevent additional damage, transcription must be attenuated proximal to broken DNA. R-Loops, a product of stalled transcription, are thought to participate in rapid

Global MS/MS Epigenetic Analysis of DNA Damage Response

repair of some DSBs arising in transcriptional units^{82,83}. We examined both RNA Polymerase II (Pol II) and R-Loops at γ H2AX foci with or without GSK126 treatment (Fig. 3e). Attenuation of H3K27 methylation resulted in an increase in Pol II and a decrease in R-Loops at γ H2AX foci 1 h PIR suggesting transcription is not properly attenuated, perhaps resulting in impeded DSB repair or leading to further damage by transcribing across broken DNA.

We next investigated the dramatic attenuation of proliferation upon GSKJ4 treatment. SA- β gal staining was conducted to assess cell senescence⁸⁴. Persistent DDR signaling can drive cells toward senescence, even in the absence of unrepaired DSBs. Cells were treated as in the IncuCyte experiment and stained for SA- β gal five days post IR exposure (Fig. S4d). These data reveal that GSKJ4 treatment, alone or in combination with EZH2 inhibition, increases cellular senescence. However, GSK126 treatment did not increase senescence. We examined γ H2AX foci 24 h PIR in combination with 1 h treatment with GSK126, JMJD2i or a combination. Indeed, exposure to GSKJ4 alone or in combination with GSK126 led to increased persistent γ H2AX foci indicative of a failure to wind down damage signaling following end joining. Persistent DSB signaling has been shown to trigger senescence^{84,85}. Thus, H3K27me3 may act at multiple stages during the DDR process. Perhaps H3K27me3 deposited at breaks is required for end joining, but must later be removed by JMJD proteins. Failure to do so triggers persistent DDR signaling leading to senescence^{86–88}.

Imaging confirms that H3K27me3 is deposited proximal to DSBs and mediates γ H2AX formation

Global MS/MS Epigenetic Analysis of DNA Damage Response

Toward confirming a local effect of H3K27 methylation at DSBs, we examined colocalization of H3K27me3 and γ H2AX after irradiation. Conventional immunofluorescence analysis 1 h PIR revealed punctate domains of increased H3K27me3 immunoreactivity along with significant overlap between H3K27me3 and γ H2AX (Fig. 4a). Colocalization analysis revealed diminished colocalization of H3K27me3 and γ H2AX after treatment with GSKJ4 or GSK126, as compared to vehicle treatment, or addition of the PARP inhibitor veliparib (Fig 4b).

To further examine H3K27me3 staining after DNA damage, we applied ground state depletion (GSD) superresolution immunofluorescence imaging at 1 h PIR, revealing punctate colocalization of H3K27me3 and γ H2AX staining to a 50 nm resolution (Fig. 4c). In order to directly assay molecular colocalization, we adapted GSD to enable detection of molecular proximity by Förster resonance energy transfer (FRET). Here, γ H2AX was detected with an anti- γ H2AX antibody coupled to a secondary antibody labeled with the donor fluorophore (DNR) and H3K27me3 with an anti-H3K27me3 antibody coupled to a secondary antibody labeled with the acceptor fluorophore (ACC). In areas where γ H2AX and H3K27me3 are in molecular proximity, DNR excitation can be transferred to ACC via FRET, quenching DNR fluorescence. Imaging γ H2AX and H3K27me3 at 1 h PIR in the DNR and ACC channels revealed similar distributions (Fig. 4d). Upon depletion of the ACC fluorophore by intense laser power, the H3K27me3 ACC signal was lost but the γ H2AX DNR signal brightened, indicating relief of FRET quenching and thus, colocalization (Fig. 4e). A pseudocolored image indicating fold increase in DNR fluorescence after ACC depletion reveals puncta of FRET signal, consistent with H3K27me3 and γ H2AX forming in molecular proximity

Global MS/MS Epigenetic Analysis of DNA Damage Response

at DSBs (Fig. 4f). Taken together, these data suggest that H3K27me3 is deposited at DSB loci and histone modifications may delineate a domain surrounding DSBs to promote detection, signaling and repair.

That a modification linked to heterochromatinization accumulates at DSBs is difficult to reconcile with purported roles for chromatin relaxation due to remodeling, PARylation and/or acetylation in γ H2AX foci formation and DSB repair^{31,35,89–92}. To examine whether DSB-associated H3K27me3 induces chromatin compaction, cells were stained for H3K27me3 and total H3 at 1 h PIR. H3K27me3 foci could be clearly distinguished, most of which did not appear to be associated with structures in the H3 image (Fig. 4g). Quantitation of the relative intensity of H3K27me3 and H3 staining indicated that H3K27me3 foci did not induce corresponding H3 foci (Fig. 4g right panel), arguing against local compaction and confirming focal deposition of H3K27me3 after irradiation. Proteomic data indicated that the increase in H3K27me3 was restricted to the H3.3 isoform (Fig 2d). To confirm that deposition of H3K27me3 was restricted to DSBs arising in euchromatin, we measured DAPI intensity underneath γ H2AX foci as a proxy for chromatin condensation. Foci in areas with low DAPI had higher H3K27me3 levels despite, presumably, a lower density of nucleosomes in these regions (Fig 4h). Thus, we concluded that deposition of repressive chromatin marks is necessary for repair of a subset of DSBs arising in euchromatin, perhaps to attenuate local transcription. Notably, some have hypothesized that heterochromatin may be refractive to DSB induction underscoring the importance of repairing euchromatic DSBs^{36,93}.

Phosphorylation of H2AX by ATM spreads kilobases away from damage sites, amplifying local signals to globally induce the DDR even from single DSBs. Thus, we

Global MS/MS Epigenetic Analysis of DNA Damage Response

621 assessed whether H3K27me3 might impact γ H2AX spreading. Comparing the size of
 622 γ H2AX foci at 1 h PIR in cells treated with vehicle, PARP inhibitor veliparib, JMJD2/4
 623 inhibitor GSKJ4, EZH2 inhibitor GSK126 or the combination of GSK126 and GSKJ4
 624 revealed that deregulation of H3K27me3 could impact γ H2AX spreading (Fig. 4i).
 625 Strikingly, inhibition of the repressive mark H3K27me3 significantly reduced the spread
 626 of γ H2AX, suggesting that PRC2 plays a role upstream of PIKKs in promoting signaling.
 627 These effects may be due to diminished H3K27me3 dependent recruitment of PRC1, a
 628 known mediator of the DDR⁹⁴. Thus, local chromatin modification may affect global DDR
 629 signaling, and ultimately, response to IR as evidenced by radiosensitization induced by
 630 EZH2 inhibitors.

631

Global MS/MS Epigenetic Analysis of DNA Damage Response

Discussion

Repair of double strand breaks is a complex process which occurs at several kinetically and spatially distinct levels in the cell. Much is known about the signaling-level events following DSB recognition (cell cycle arrest, transcriptional changes) and the downstream consequences of failure to repair DNA damage (apoptosis, senescence). However, chromatin-level changes in histone modifications which direct recognition and repair of DSBs are understudied. Indeed, DSBs are, by definition, a chromatin-localized event. Here, we report a global survey of changes to histone PTMs following DNA damage induced via ionizing radiation.

Analysis of histone PTMs after IR insult was carried out by AMT based MS/MS analysis and revealed widespread changes to the epigenome which persisted up to 48 h after IR. Modifications across all major histones were altered including modifications known to be key mediators of cell development such as H4 acetylation and H3K4 methylation. Clustering of PTM trajectories suggested at least two kinetically separate patterns of histone PTM alteration, one rapid and one occurring over ~24 hours. We chose to focus on PTMs altered at 1 h PIR as later-occurring changes are increasingly likely to be mediated by cell cycle stoppage or transcriptional alteration following IR. Our analysis recapitulated several PTMs previously linked to DNA repair including H3K79me2, H3K27me3 and acetylation of the H4 tail. By assessing non-canonical PTMs via targeted PTM search for other known histone modifications we expanded the repertoire of DDR associated PTMs to include 17 types of modifications (across 3076 sites). Furthermore, though we detected small fold changes for many PTMs in our study we believe this to be reflective of larger, DSB-proximal changes diluted out by whole-

Global MS/MS Epigenetic Analysis of DNA Damage Response

chromatin analysis. Enrichment of DSB-proximal chromatin could be used to confirm our findings and definitively segregate local PTM alterations from global changes after irradiation.

Changes in other PTMs notwithstanding, we focused on alterations of H3K27 methylation and their relationship to DNA damage repair. Using MRM targeted analysis, we detected increased H3K27me3 levels following IR. We are not the first to suggest that H3K27 methylation impacts repair of DNA damage; others have presented conflicting evidence as to whether H3K27me3 or its writer, PRC2, are localized to DSBs^{44,45,95}. However, to our knowledge, we are the first to use FRET imaging to localize H3K27me3 deposited on DSB proximal nucleosomes. We further suggest that H3K27me3 is a critical regulator of the DDR. Inhibition of the H3K27 methyltransferase EZH2 or the opposing demethylase, JMJD2, sensitized cells to radiation via distinct mechanisms. Blocking H3K27me3 deposition delayed break repair, while inhibiting the removal of K27 methylation precluded attenuation of DDR signaling, leading to senescence. Thus, inhibitors of H3K27 methylation are putative radiosensitizers warranting further study perhaps in an *in vivo* setting.

Towards a mechanism for H3K27 methylation in the DDR, we examined γ H2AX foci establishment in the presence of H3K27 methylation inhibitors. Inhibition of either EZH2 or its counterpart JMJD2 attenuated γ H2AX foci number and intensity shortly after IR insult. These data place histone modification upstream of DSB recognition by PIKKs, key mediators of downstream DDR signaling. While H3K27 trimethylation is sometimes associated with heterochromatin, EZH2 has been linked to facultative repression of genes even in non-condensed chromatin. This is in line with work which

Global MS/MS Epigenetic Analysis of DNA Damage Response

suggests that EZH2 may function to repress transcription proximal to DSB loci, thus preventing transcription across broken DNA. In our hands, we observed accumulation of H3K27me3 surrounding DSB loci without a concomitant increase histone occupancy. Thus, at early time points, DSB proximal chromatin compaction may not occur despite deposition of repressive marks. Perhaps H3K27me3 is a permissive mark which defines the DSB repair domain, or it may be required for deposition of γ H2AX possibly via recruitment of ATM or another repair factors.

A role for EZH2 in preventing transcription-damage conflicts suggests that EZH2 may be specifically deposited in genic regions which sustain DNA damage. Consistent with this hypothesis, isoform-selective methylation of H3K27 following IR was observed by targeted proteomics. H3.3, an H3 isoform associated with euchromatin, realized the bulk of the increase in H3K27me3. Further, via imaging, we observed relatively stronger induction of H3K27me3 at DSBs in areas of open chromatin, likely euchromatin. Additionally, we place H3K27me3 upstream of R-Loop formation and show that inhibiting EZH2 prevents attenuation of Pol II at DSBs. Collectively, these data raise the possibility that different genomic regions may require distinct repair programs dependent upon their basal epigenetic state. By extension, the role of histone marks in directing DSB repair may be distinct from their basal location or activity.

It is interesting, and indeed apparently paradoxical, that either increased or decreased DSB-proximal H3K27me3 levels are sufficient to attenuate γ H2AX deposition. However, we note that inhibition of EZH2 or JMJD2 evinced different phenotypes, with only the latter accelerating cellular senescence. Additionally, we posit that our findings could be evidence of a multistep process of histone methylation at

Global MS/MS Epigenetic Analysis of DNA Damage Response

DSBs which is separated either kinetically or spatially. For example, it may be that H3K27me3 deposition is necessary for repair in euchromatin, but this excess methylation must later be removed to restore basal chromatin activity. Failure to restore the basal epigenetic state may prolong DDR signaling and contribute to senescence. Indeed, altering H3K27me3 levels has been shown to induce senescence in the absence of DNA damage⁹⁶. Our data is also consistent with reports that the H3 demethylase UTX is required for the DDR⁹⁷. Returning to the influence of basal epigenetic states on the DDR, loci in different epigenetic states may be repaired via distinct epigenetic mechanisms or at different times following IR. This is consistent with the separable kinetics of histone modifications observed in our proteomics data. Future studies must address the relationship between preexisting chromatin state, repair pathway and repair kinetics. For example, many studies note special repair pathways and activities for heterochromatic regions or telomeric chromatin^{30,98}.

Our findings also suggest a more fundamental purpose of highly conserved epigenetic readers and writers such as the polycomb family. PRC2 was first identified in flies and is highly conserved even in organisms which lack complex gene expression control^{99,100}. Yet, all eukaryotes have DNA repair systems to repair breaks and safeguard genetic information. Therefore, it is likely that the DDR activity of PRC2 and other enzymes does not represent moonlighting, but rather is an essential and ancient subset of their functions. A fuller understanding of how these enzymes function in DSB repair may, in turn, shed light on their roles in transcription. Transcription-coupled repair of DSBs has been postulated, as has transcriptional damage to DNA^{101,102}. This study

Global MS/MS Epigenetic Analysis of DNA Damage Response

723 reframes these concepts by suggesting transcription-independent roles for
724 transcriptional machinery in the DDR.

Global MS/MS Epigenetic Analysis of DNA Damage Response

Data Availability

All data and code used to generate figures are available upon request to the corresponding author. Epiprofile proteomics data have been deposited to the ProteomeXchange Consortium via the PRIDE partner repository⁶² with the dataset identifier PXD019388. EHMP data is attached to this manuscript.

Acknowledgements

We thank Jacek Sikora (now at AbbVie) and the staff of Northwestern Proteomics and Ken Johnson and the staff of the Mayo Clinic Proteomics Core for proteomics support and Vytas Bindokas and Christine Labno of the University of Chicago Integrated Light Microscopy Core for training and consultation.

Grant Funding

This work was supported by NCI grants R21 CA213247 and R01 CA199663 and by DoD CDMRP PRCRP Impact Award CA190982 to SJK. JL was partially supported by the Multi-disciplinary Training program in Cancer Research (MTCR), T32 CA009594. The Integrated Light Microscopy Core was supported by NCI cancer center grant P30 CA014599. Northwestern Proteomics was supported by P30 CA060553 and P41 GM108569.

Contributions

Global MS/MS Epigenetic Analysis of DNA Damage Response

J.L. conceived the experiments, performed experiments, obtained and analyzed images, assembled the data and wrote the manuscript. D.W. prepared proteomic samples, analyzed LC-MS/MS data and helped prepare the manuscript. S.K. supervised the study. All authors read and approved the final manuscript.

Ethics declarations

The authors declare no competing interests

Supplemental Data

This article contains supplemental data.

Global MS/MS Epigenetic Analysis of DNA Damage Response

Figure Legends

Figure 1 Histone post-translational modifications (PTMs) are dynamically altered by DNA damage induction

a) tSNE of samples from MRM histone PTM time-course analysis. Dots represent samples from technical replicates ($n = 3$), color-coded to denote the timepoint after exposure to mock-irradiated (NIR) or 6 Gy (IR), using a ^{60}Co γ -ray source. Data used to compute the tSNE are histone PTM per-residue percentages from the EHMP assay.

b) Heatmap of the matrix used to generate the tSNE plot in Fig.1a. Heatmap is clustered by Euclidian distance between samples. Data used are histone PTM per-residue percentages from the EHMP assay. Three replicates are shown.

c) Centroid plots of histone PTM clusters. Data used are histone PTM per-residue percentages from the EHMP assay, averaged between three replicates. Average trajectories of all PTMs were clustered according to their Dynamic Time Warping distance and then centroids were fitted and plotted by the PAM algorithm. The number of clusters was set to 5 after manual inspection of the data. The Y-axis denotes the relative average PTM density in each cluster normalized to the NIR timepoint.

d) Volcano Plot of all PTMs analyzed. X-axis denotes the average fold change between the NIR and 1 h PIR timepoints. Y-axis shows the negative log of the FDR corrected P-value. Points are color-coded according to their significance at 5% FDR (comparison of NIR to 1 hPIR by Wilcox Ranked-Sum Test) and their shape denotes the significance

Global MS/MS Epigenetic Analysis of DNA Damage Response

for a Kruskal-Wallis test across all timepoints, also at 5% FDR. H3K27me3 is labeled for clarity.

Figure 2 Epiprofile 2.0 quantification of temporal histone marks after DNA damage induction

a) Heatmap of the relative changes between timepoints for PTMs on Histone H3 and Histone H4. Data are the average percent PTM change between NIR samples and the indicated timepoints. Data from biological replicates ($n = 3$). Note the time-point specific regulation of various groups of marks.

b) Plot shows average modification changes for acetyl, mono-, di-, and tri-methylation across all residues measured for each of the timepoints relative to NIR. Data from biological replicates ($n = 3$). We observe a decrease in acetylation following IR and an increase in overall methylation specifically me2 and me3 at the 1 h PIR timepoint. Error bars show SEM between average PTM values. Significance was determined by Wilcoxon Ranked-Sum Test between indicated timepoints. Significance values are as follows: ns $p > 0.05$; * $p < 0.05$; ** $p < 0.01$; *** $p < 0.001$; **** $p < 0.0001$. Total number of PTMs are: Ac-13, me1-13, me2-7, me-3 7.

c) Abundance of H3K27 di-methylation separated by H3 isoforms at 1 and 4 h PIR. Plot shows the percent of the residue in each modification state. The magnitude of changes is much larger for H3.3, an isoform associated with euchromatin. Error bars show SEM between average PTM values across biological replicates ($n = 3$).

Global MS/MS Epigenetic Analysis of DNA Damage Response

d) Abundance of H3K27 tri-methylation separated by H3 isoforms at 1 and 4 h PIR. Plot shows the percent of the residue in each modification state. The magnitude of changes is much larger for H3.3, an isoform associated with euchromatin. Error bars show SEM between average PTM values across biological replicates ($n = 3$).

Figure 3 Inhibition of H3K27 methylation attenuates DSB recognition and repair

a) Mean number of γ H2AX foci after drug treatment. Foci counting was performed by a custom ImageJ macro. Drugs were added for the indicated length of time prior to dosing with 6Gy of IR. Cells were fixed and stained 1 h PIR. Combo refers to a mixture of both GSK126 and GSKJ4 at their original concentrations. Significance was determined by a Kruskal-Wallis test performed within each treatment group. Significance values are as follows: ns $p > 0.05$; * $p < 0.05$; ** $p < 0.01$; *** $p < 0.001$; **** $p < 0.0001$. Three biological replicates were collected. Total number of points are: 86, 33, 37, 90, 21, 39, 84, 21, 25, 62, 29, 36 per group from left to right.

b) Plot as in Fig. 3b but showing the mean γ H2AX foci intensity. Foci intensity analysis was performed by a custom ImageJ macro. Three biological replicates were collected. Significance testing as in Fig. 3a. Total number of points are: 86, 33, 37, 90, 21, 39, 84, 21, 25, 62, 29, 36 per group from left to right.

c) Comet assay results of cells treated as in Fig. 3b and assayed either 1 or 24 h PIR. Plotted is the Tail DNA percent as reported by the ImageJ plugin OpenComet. Significance was determined by a Wilcoxon Ranked-Sum Test against DMSO treatment.

Global MS/MS Epigenetic Analysis of DNA Damage Response

821 Three biological replicates were collected. Total number of points are: 78, 103, 67, 94,
822 55, 80, 52, 68 from left to right.

823 d) Mean fluorescence intensity of the indicated antigens at γ H2AX foci. Foci intensity
824 analysis was performed by a custom ImageJ macro. Three biological replicates were
825 collected. Total number of points are as follows: 1210, 416, 2790, 2738 from left to right

826 e) Plot as in Fig. 3a, but performed 24 h PIR. Foci counting was performed by a custom
827 ImageJ macro. Drugs were added for 1 h prior to dosing with 6 Gy of IR and media was
828 exchanged 1 h after IR insult. Three biological replicates were collected. Total number
829 of points are as follows: 144, 142, 151, 149 from left to right

830

831 **Figure 4 H3K27me3 is a local determinant of DSB recognition**

832 a) Immunofluorescence images of irradiated MCF7 cells. Cells were treated with the
833 indicated drugs for 60 minutes prior to dosing with 6 Gy. Cells were fixed and stained 1
834 h PIR. Images were acquired using a 40 X oil objective on a spinning-disk confocal
835 microscope. A representative image is shown from 3 replicates.

836 b) Quantification of colocalization between γ H2AX and H3K27me3 staining in the slides
837 shown in Fig. 4a. The fraction of colocalized pixels was calculated per nucleus using
838 Li's ICA method. Significance was determined by a Wilcox Ranked-Sum Test against
839 DMSO treatment. Significance values are as follows: ns $p > 0.05$; * $p < 0.05$; ** $p < 0.01$; ***
840 $p < 0.001$; **** $p < 0.0001$. Three biological replicates were collected. Total number of
841 datapoints are as follows: 165, 56, 45, 41, 31 per group from left to right.

Global MS/MS Epigenetic Analysis of DNA Damage Response

- 842 c) Superresolution imaging of irradiated MCF7 cells. DMSO treated cells were fixed 1 h
843 PIR and imaged on a Leica GSD imaging system. Inset shows colocalized puncta of
844 H3K27me3 and γ H2AX. A representative image is shown from 3 replicates.
- 845 d) GSD-FRET analysis of colocalization between γ H2AX and H3K27me3. DMSO
846 treated cells were fixed 1 h PIR and imaged on a Leica GSD imaging system using a
847 160x objective. Both Donor and Acceptor channels were imaged at their respective
848 excitation maxima. A representative image is shown from 3 replicates.
- 849 e) Cells as in Fig. 4d but following depletion of the Acceptor fluorescent dye using
850 intense laser power for 2 minutes. Imaging conditions were equivalent to Fig. 4d.
- 851 f) Pseudo colored image showing the relative increase in signal in the Donor channel
852 following Acceptor photobleach (Fig. 4e, left minus Fig. 4d, left). Inset shows region with
853 both γ H2AX and H3K27me3 signal from panel Fig. 4d alongside the same region from
854 Fig. 4f.
- 855 g) Ratio-based imaging of irradiated MCF7 cells. Cells were fixed 1 h PIR and imaged
856 using a 40 X oil objective on a spinning-disk confocal microscope. Ratios between
857 channels were calculated in ImageJ by dividing image intensities and then the resulting
858 image was thresholded. Rightmost panel was pseudo-colored to highlight differences in
859 H3K27me3:H3 ratio. A representative image is shown from 3 replicates.
- 860 h) Mean fluorescence intensity of H3K27me3 at γ H2AX foci after GSK126 treatment.
861 Drugs were added for 1 h prior to IR. Cells were fixed and stained 1 h PIR. Foci
862 intensity analysis was performed by a custom ImageJ macro. γ H2AX foci were
863 thresholded and the MFI within foci areas in the H3K27me3 channel was recorded.

Global MS/MS Epigenetic Analysis of DNA Damage Response

Subsequently, data was divided with respect to the DAPI intensity within foci area. DAPI-High indicates regions with a DAPI intensity greater than the cell-wide mean. Significance was determined by a Wilcox Ranked-Sum Test against DMSO treatment. Significance values are as follows: ns $p > 0.05$; * $p < 0.05$; ** $p < 0.01$; *** $p < 0.001$; **** $p < 0.0001$. Three biological replicates were collected. Total number of datapoints are as follows: 1342, 1644 per group from left to right.

i) Plot of the size of γ H2AX foci in drug-treated MCF7 cells. Cells were treated with the indicated drugs for 60 minutes prior to dosing with 6 Gy. Cells were fixed and stained 1 h PIR. Images were acquired using a 40 X oil objective on a spinning-disk confocal microscope. Size of individual γ H2AX foci were determined using a custom ImageJ macro. Significance was determined by a Wilcox Ranked-Sum Test against DMSO treatment. Significance values are as follows: ns $p > 0.05$; * $p < 0.05$; ** $p < 0.01$; *** $p < 0.001$; **** $p < 0.0001$. Three biological replicates were collected. Total number of datapoints are as follows: 518, 516, 513, 505, 520 per group from left to right.

Supplemental Figures:

Figure S1 EHMP analysis reveals several Histone PTMs are altered following IR

a) Select H3 and H4 residue PTM data from the EHMP survey are shown. Height of the bars represents the percent of the residue modified at the indicated timepoint. Error bars show standard deviation for three replicates. Significance was determined by a Kruskal-Wallis test comparing timepoints within a given residue. Significance values are as follows: ns $p > 0.05$; * $p < 0.05$; ** $p < 0.01$; *** $p < 0.001$; **** $p < 0.0001$.

Global MS/MS Epigenetic Analysis of DNA Damage Response

886

887 **Figure S2 EpiProfiler confirms IR mediated changes to histone PTMs**

888 a) Select H3 and H4 residue PTM data from the EpiProfiler Histone PTM dataset are
 889 shown. Height of the bars represents the percent of the residue modified at the
 890 indicated timepoint. Error bars show standard deviation for three replicates. Significance
 891 was determined by a Friedman test comparing timepoints within a given residue.
 892 Significance values are as follows: ns $p > 0.05$; * $p < 0.05$; ** $p < 0.01$; *** $p < 0.001$; ****
 893 $p < 0.0001$.

894

895 **Figure S3 EHMP and EpiProfile analyses report differential histone alterations**

896 a) Matrix shows the correlation between 55 PTMs measured by both EpiProfile and the
 897 EHMP assay. Color of the squares is proportional to Pearson's correlation coefficient.
 898 The R^2 value between two timepoints is shown within each square. Data used to
 899 construct the matrix are the average percent residue modification values.

900

901 **Figure S4 Inhibition of H3K27 methylation sensitizes cells to Ionizing Radiation**

902 a) H3K27me3 mean fluorescent intensity of drug treated cells. Cells were treated and
 903 imaged as in Fig. 3b. MFI is calculated for each nucleus using a custom ImageJ macro.
 904 Significance was determined by a Wilcoxon Ranked-Sum Test against DMSO treatment.
 905 Significance values are as follows: ns $p > 0.05$; * $p < 0.05$; ** $p < 0.01$; *** $p < 0.001$; ****
 906 $p < 0.0001$. Three biological replicates were collected. Total number of datapoints are as
 907 follows: 110, 62, 43, 49, 38 per group from left to right.

Global MS/MS Epigenetic Analysis of DNA Damage Response

908 b) Incucyte growth curves of drug treated cells. Cells were treated for 60 min as in Fig.
 909 3b and then exposed to IR or mock irradiated (NIR). Cell number was tracked for 120 h
 910 in an Incucyte system. The mean normalized number of cells is plotted, and error bars
 911 denote SEM for 3 replicates. Significance was determined by Dunnett's Multiple
 912 Comparisons Test against DMSO treatment.

913 c) Images excerpted from the Incucyte image dataset over the course of the 120 h
 914 analysis. Timepoints are equivalent to Fig. 3d. Only the IR condition is shown.

915 d) SA- β Gal staining of cells treated for 1 h with the indicated drugs prior to IR insult and
 916 allowed to recover for 72 h before fixation and staining. A representative image,
 917 selected from three replicates, is shown for each treatment.

918

Global MS/MS Epigenetic Analysis of DNA Damage Response

References

1. Pilié, P. G., Tang, C., Mills, G. B. and Yap, T. A. State-of-the-art strategies for targeting the DNA damage response in cancer. *Nature Reviews Clinical Oncology* 16, 81–104 (2018).
2. Lomax, M. E., Folkes, L. K. and O'Neill, P. Biological Consequences of Radiation-induced DNA Damage: Relevance to Radiotherapy. *Clinical Oncology* 25, 578–585 (2013).
3. Orth, M., Lauber, K., Niyazi, M., Friedl, A. A., Li, M., Maihöfer, C., Schüttrumpf, L., Ernst, A., Niemöller, O. M. and Belka, C. Current concepts in clinical radiation oncology. *Radiation and Environmental Biophysics* 53, 1–29 (2014).
4. Xiao, Y. and Rosen, M. The role of Imaging and Radiation Oncology Core for precision medicine era of clinical trial. *Translational Lung Cancer Research* 6, 621–624 (2017).
5. Conibear, J. Rationale for concurrent chemoradiotherapy for patients with stage III non-small-cell lung cancer. *British Journal of Cancer* 123, 10–17 (2020).
6. Machtay, M., Moughan, J., Trotti, A., Garden, A. S., Weber, R. S., Cooper, J. S., Forastiere, A. and Ang, K. K. Factors Associated With Severe Late Toxicity After Concurrent Chemoradiation for Locally Advanced Head and Neck Cancer: An RTOG Analysis. *Journal of Clinical Oncology* 26, (2021).
7. Du, C., Ying, H., Kong, F., Zhai, R. and Hu, C. Concurrent chemoradiotherapy was associated with a higher severe late toxicity rate in nasopharyngeal carcinoma patients compared with radiotherapy alone: a meta-analysis based on randomized controlled trials. *Radiation Oncology* 10, 70 (2015).

Global MS/MS Epigenetic Analysis of DNA Damage Response

- 942 8. Curtin, N. J. DNA repair dysregulation from cancer driver to therapeutic target.
943 Nature Reviews Cancer 12, 801–817 (2012).
- 944 9. De Schutter, H. and Nuyts, S. Radiosensitizing potential of epigenetic anticancer
945 drugs. Anti-cancer agents in medicinal chemistry 9, 99–108 (2009).
- 946 10. Jachimowicz, R. D., Goergens, J. and Reinhardt, H. C. DNA double-strand break
947 repair pathway choice - from basic biology to clinical exploitation. Cell Cycle vol. 18
948 1423–1434 (2019).
- 949 11. Sonnenblick, A., De Azambuja, E., Azim, H. A. and Piccart, M. An update on
950 PARP inhibitors—moving to the adjuvant setting. Nature Publishing Group, 12, 27–41
951 (2014).
- 952 12. D’Andrea, A. D. Mechanisms of PARP inhibitor sensitivity and resistance. DNA
953 Repair 71:172-176 (2018).
- 954 13. Clouaire, T. and Legube, G. A Snapshot on the Cis Chromatin Response to DNA
955 Double-Strand Breaks. Trends in Genetics 35, 330–345 (2019).
- 956 14. Yamamori, T., Yasui, H., Yamazumi, M., Wada, Y., Nakamura, Y., Nakamura, H.
957 and Inanami, O. Ionizing radiation induces mitochondrial reactive oxygen species
958 production accompanied by upregulation of mitochondrial electron transport chain
959 function and mitochondrial content under control of the cell cycle checkpoint. Free
960 Radical Biology and Medicine 53, 260–270 (2012).
- 961 15. Rogakou, E. P., Pilch, D. R., Orr, A. H., Ivanova, V. S. and Bonner, W. M. DNA
962 double-stranded breaks induce histone H2AX phosphorylation on serine 139. The
963 Journal of biological chemistry 273, 5858–68 (1998).

Global MS/MS Epigenetic Analysis of DNA Damage Response

- 964 16. Paull, T. T., Rogakou, E. P., Yamazaki, V., Kirchgessner, C. U., Gellert, M. and
965 Bonner, W. M. A critical role for histone H2AX in recruitment of repair factors to nuclear
966 foci after DNA damage. *Current Biology* 10, 886–895 (2000).
- 967 17. Rothkamm, K., Barnard, S., Moquet, J., Ellender, M., Rana, Z. and
968 Burdak-Rothkamm, S. DNA damage foci: Meaning and significance. *Environmental and*
969 *molecular mutagenesis* 56, 491–504 (2015).
- 970 18. Belyaev, I. Y. Radiation-induced DNA repair foci: spatio-temporal aspects of
971 formation, application for assessment of radiosensitivity and biological dosimetry.
972 *Mutation Research/Reviews in Mutation Research* 704, 132–141 (2010).
- 973 19. Bai, P. Biology of Poly(ADP-Ribose) Polymerases: The Factotums of Cell
974 Maintenance. *Molecular Cell* 58, 947–958 (2015).
- 975 20. Gupte, R., Liu, Z. and Kraus, W. L. PARPs and ADP-ribosylation: Recent
976 advances linking molecular functions to biological outcomes. *Genes and Development*
977 31, 101–126 (2017).
- 978 21. Skidmore, C. J., Davies, M. I., Goodwin, P. M., Halldorsson, H., Lewis, P. J.,
979 Shall, S. and Zia'ee, A. A. The Involvement of Poly(ADP-ribose) Polymerase in the
980 Degradation of NAD Caused by γ -Radiation and N-Methyl-N-Nitrosourea. *European*
981 *Journal of Biochemistry* 101, 135–142 (1979).
- 982 22. Chapman, J. R., Taylor, M. R. G. and Boulton, S. J. Playing the End Game: DNA
983 Double-Strand Break Repair Pathway Choice. *Molecular Cell* 47, 497–510 (2012).
- 984 23. Ceccaldi, R., Rondinelli, B. and D'Andrea, A. D. Repair Pathway Choices and
985 Consequences at the Double-Strand Break. *Trends in Cell Biology* vol. 26 52–64
986 (2016).

Global MS/MS Epigenetic Analysis of DNA Damage Response

- 987 24. Panier, S. and Boulton, S. J. Double-strand break repair: 53BP1 comes into
988 focus. *Nature Reviews Molecular Cell Biology* 15, 7–18 (2013).
- 989 25. Jackson, S. P. and Bartek, J. The DNA-damage response in human biology and
990 disease. *Nature* 461, 1071–1078 (2009).
- 991 26. Blackford, A. N. and Jackson, S. P. Molecular Cell Review ATM, ATR, and DNA-
992 PK: The Trinity at the Heart of the DNA Damage Response. *Molecular Cell* 66, 801–817
993 (2017).
- 994 27. Arnoult, N., Correia, A., Ma, J., Merlo, A., Garcia-Gomez, S., Maric, M., Tognetti,
995 M., Benner, C. W., Boulton, S.J., Saghatelian, A. and Karlseder, J. Regulation of DNA
996 repair pathway choice in S and G2 phases by the NHEJ inhibitor CYREN. *Nature* 549,
997 548–552 (2017).
- 998 28. Jeggo, P. A., Downs, J. A. and Gasser, S. M. Chromatin modifiers and
999 remodelers in DNA repair and signaling. *Philosophical Transactions of the Royal*
1000 *Society B: Biological Sciences* 372, 20160279 (2017).
- 1001 29. Hunt, Clayton R., Deepti Ramnarain, Nobuo Horikoshi, Puneeth Iyengar, Raj K.
1002 Pandita, Jerry W. Shay, and Tej K. Pandita. Histone Modifications and DNA Double-
1003 Strand Break Repair after Exposure to Ionizing Radiations. *Radiation Research* 179,
1004 383–392. 2013.
- 1005 30. Chiolo, I., Caridi, P. C., Delabaere, L. and Zapotoczny, G. And yet, it moves:
1006 nuclear and chromatin dynamics of a heterochromatic double- strand break.
1007 *Philosophical transactions of the Royal Society of London. Series B, Biological sciences*
1008 372, (2017).

Global MS/MS Epigenetic Analysis of DNA Damage Response

- 1009 31. Burgess, R. C., Burman, B., Kruhlak, M. J. and Misteli, T. Activation of DNA
1010 Damage Response Signaling by Condensed Chromatin. *Cell Reports* 9, 1703–1718
1011 (2014).
- 1012 32. Delgoffe, Greg M., Kristen N. Pollizzi, Adam T. Waickman, Emily Heikamp, David
1013 J. Meyers, Maureen R. Horton, Bo Xiao, Paul F. Worley, Jonathan D. Powell. The
1014 kinase mTOR regulates the differentiation of helper T cells through the selective
1015 activation of signaling by mTORC1 and mTORC2. *Nature immunology* 12, 295–303
1016 (2011).
- 1017 33. Ségurel, L. and Bon, C. Recent Advancements in DNA Damage–Transcription
1018 Crosstalk and High-Resolution Mapping of DNA Breaks. *Annu. Rev. Genome Human*
1019 *Genetics* 18, 87–113 (2017).
- 1020 34. Lavelle, C. and Foray, N. Chromatin structure and radiation-induced DNA
1021 damage: From structural biology to radiobiology. *International Journal of Biochemistry*
1022 *and Cell Biology* 49, 84–97 (2014).
- 1023 35. Dellaire, G., Kepkay, R. and Bazett-Jones, D. P. High resolution imaging of
1024 changes in the structure and spatial organization of chromatin, γ -H2A.X and the MRN
1025 complex within etoposide-induced DNA repair foci. *Cell Cycle* 8, 3750–3769 (2009).
- 1026 36. Kim, J. A., Kruhlak, M., Dotiwala, F., Nussenzweig, A. and Haber, J. E.
1027 Heterochromatin is refractory to γ -H2AX modification in yeast and mammals. *Journal of*
1028 *Cell Biology* 178, 209–218 (2007).
- 1029 37. Murga, M., Jaco, I., Fan, Y., Soria, R., Martinez-Pastor, B., Cuadrado, M., Yang,
1030 S.M., Blasco, M. A., Skoultchi, A. I. and Fernandez-Capetillo, O. Global chromatin

Global MS/MS Epigenetic Analysis of DNA Damage Response

- 1031 compaction limits the strength of the DNA damage response. *Journal of Cell Biology*
- 1032 178, 1101–1108 (2007).
- 1033 38. Takata, H., Hanafusa, T., Mori, T., Shimura, M., Iida, Y., Ishikawa, K.,
- 1034 Yoshikawa, K., Yoshikawa, Y. and Maeshima, K. Chromatin Compaction Protects
- 1035 Genomic DNA from Radiation Damage. *PLoS ONE* 8, 1–11 (2013).
- 1036 39. Spothem-Maurizot, M., Ruiz, S., Sabattier, R. and Charlier, M. Radioprotection
- 1037 of DNA by Polyamines. *International Journal of Radiation Biology* 68, 571–577 (1995).
- 1038 40. Schuettengruber, B., Bourbon, H. M., Croce, L. Di and Cavalli, G. Leading Edge
- 1039 Review Genome Regulation by Polycomb and Trithorax: 70 Years and Counting. *Cell*
- 1040 171, 34–57 (2017).
- 1041 41. van Kruijsbergen, I., Hontelez, S. and Veenstra, G. J. C. Recruiting polycomb to
- 1042 chromatin. *International Journal of Biochemistry and Cell Biology* 67, 177–187 (2015).
- 1043 42. di Croce, L. and Helin, K. Transcriptional regulation by Polycomb group proteins.
- 1044 *Nature Structural and Molecular Biology* 20, 1147–1155 (2013).
- 1045 43. Aranda, S., Mas, G. and di Croce, L. Regulation of gene transcription by
- 1046 Polycomb proteins. *Science Advances* 1, 1–16 (2015).
- 1047 44. Campbell, S., Ismail, I. H., Young, L. C., Poirier, G. G. and Hendzel, M. J.
- 1048 Polycomb repressive complex 2 contributes to DNA double-strand break repair. *Cell*
- 1049 *Cycle* 12, 2675–2683 (2013).
- 1050 45. Chou, D. M., Adamson, B., Dephoure, N. E., Tan, X., Nottke, A. C., Hurov, K. E.,
- 1051 Gygi, S. P., Colaiácovo, M. P. and Elledge, S. J. A chromatin localization screen reveals
- 1052 poly (ADP ribose)-regulated recruitment of the repressive polycomb and NuRD

Global MS/MS Epigenetic Analysis of DNA Damage Response

- 1053 complexes to sites of DNA damage. Proceedings of the National Academy of Sciences
- 1054 107, 18475–18480 (2010).
- 1055 46. Clouaire, T., Rocher, V., Lashgari, A., Arnould, C., Aguirrebengoa, M., Biernacka,
- 1056 A., Skrzypczak, M., Aymard, F., Fongang, B., Dojer, N. and Iacovoni, J.S.
- 1057 Comprehensive Mapping of Histone Modifications at DNA Double-Strand Breaks
- 1058 Deciphers Repair Pathway Chromatin Signatures. Molecular Cell 72, 250-262. (2018).
- 1059 47. Piunti, A. and Shilatifard, A. The roles of Polycomb repressive complexes in
- 1060 mammalian development and cancer. Nature Reviews Molecular Cell Biology 22, 326–
- 1061 345 (2021).
- 1062 48. Zhang Y., Chang J. F., Sun J., Chen L., Yang X. M., Tang H. Y., Jing Y. Y., Kang
- 1063 X, He Z. M., Wu J. Y., and Wei H. M. Histone H3K27 methylation is required for NHEJ
- 1064 and genome stability by modulating the dynamics of FANCD2 on chromatin. Journal of
- 1065 cell science 131.12 (2018).
- 1066 49. Efimova E. V, Takahashi S, Shamsi N. A., Wu D., Labay E, Ulanovskaya OA,
- 1067 Weichselbaum RR, Kozmin SA, Kron SJ. DNA Damage and Repair Linking Cancer
- 1068 Metabolism to DNA Repair and Accelerated Senescence. Mol Cancer Res 173-184
- 1069 (2016)
- 1070 50. Caruso L. B., Martin K. A., Lauretti E., Hulse M., Siciliano M., Lupey-Green L.N.,
- 1071 Abraham A., Skorski T., Tempera I. Poly(ADP-ribose) Polymerase 1, PARP1, modifies
- 1072 EZH2 and inhibits EZH2 histone methyltransferase activity after DNA damage.
- 1073 Oncotarget 9, 10585–10605 (2018).

Global MS/MS Epigenetic Analysis of DNA Damage Response

- 1074 51. Li J, Hart R. P., Mallimo E. M., Swerdel M. R., Kusnecov A. W., Herrup K. EZH2-
1075 mediated H3K27 trimethylation mediates neurodegeneration in ataxia-telangiectasia.
1076 Nature Neuroscience 16,1745-53. (2013).
- 1077 52. Wang Y., Sun H., Wang J., Wang H., Meng L., Xu C., Jin M., Wang B., Zhang Y.,
1078 Zhu T. DNA-PK-mediated phosphorylation of EZH2 regulates the DNA damage-induced
1079 apoptosis to maintain T-cell genomic integrity. Cell Death and Disease 7, 1–10 (2016).
- 1080 53. Finlay, M. R. V. and Griffin, R. J. Modulation of DNA repair by pharmacological
1081 inhibitors of the PIKK protein kinase family. Bioorganic and Medicinal Chemistry Letters
1082 22, 5352–5359 (2012).
- 1083 54. Bryant H. E., Schultz N., Thomas H. D., Parker K. M., Flower D., Lopez E., Kyle
1084 S., Meuth M., Curtin N. J., Helleday T. Specific killing of BRCA2-deficient tumours with
1085 inhibitors of poly(ADP-ribose) polymerase. Nature 434, 913–917 (2005).
- 1086 55. Garcia B. A., Mollah S., Ueberheide B. M., Busby S. A., Muratore T. L.,
1087 Shabanowitz J., Hunt D. F. Chemical derivatization of histones for facilitated analysis by
1088 mass spectrometry. Nature Protocols 2, 933–938 (2007).
- 1089 56. MacLean B., Tomazela D. M., Shulman N., Chambers M., Finney G. L., Frewen
1090 B., Kern R., Tabb D. L., Liebler D. C., MacCoss M. J. Skyline: An open source
1091 document editor for creating and analyzing targeted proteomics experiments.
1092 Bioinformatics 26, 966–968 (2010).
- 1093 57. Yuan Z. F., Liu C., Wang H. P., Sun R. X., Fu Y., Zhang J. F., Wang L. H., Chi
1094 H., Li Y., Xiu L. Y., Wang W. P. pParse: A method for accurate determination of
1095 monoisotopic peaks in high-resolution mass spectra. Proteomics 12, 226–235 (2012).

Global MS/MS Epigenetic Analysis of DNA Damage Response

- 1096 58. Yuan Z. F., Sidoli S., Marchione D. M., Simithy J., Janssen K. A., Szurgot M. R.,
1097 Garcia B. A. EpiProfile 2.0: A Computational Platform for Processing Epi-Proteomics
1098 Mass Spectrometry Data. *Journal of Proteome Research* 17, 2533–2541 (2018).
- 1099 59. Yuan Z. F., Lin S., Molden R. C., Cao X. J., Bhanu N. V., Wang X., Sidoli S., Liu
1100 S., Garcia B. A. EpiProfile Quantifies Histone Peptides with Modifications by Extracting
1101 Retention Time and Intensity in High-resolution Mass Spectra. *Molecular and Cellular
1102 Proteomics* 14, 1696–1707 (2015).
- 1103 60. Tyanova S., Temu T., Sinitcyn P., Carlson A., Hein M. Y., Geiger T., Mann M.,
1104 Cox J. The Perseus computational platform for comprehensive analysis of (prote)omics
1105 data. *Nature Methods* 13, 731–740 (2016).
- 1106 61. Deutsch E. W., Bandeira N., Sharma V., Perez-Riverol Y., Carver J. J., Kundu D.
1107 J, García-Seisdedos D., Jarnuczak A. F., Hewapathirana S., Pullman B. S., Wertz J.
1108 The ProteomeXchange consortium in 2020: Enabling “big data” approaches in
1109 proteomics. *Nucleic Acids Research* 48, D1145–D1152 (2020).
- 1110 62. Perez-Riverol Y., Csordas A., Bai J., Bernal-Llinares M., Hewapathirana S.,
1111 Kundu D. J., Inuganti A., Griss J., Mayer G., Eisenacher M., Pérez E. The PRIDE
1112 database and related tools and resources in 2019: Improving support for quantification
1113 data. *Nucleic Acids Research* 47, D442–D450 (2019).
- 1114 63. Gyori, B. M., Venkatachalam, G., Thiagarajan, P. S., Hsu, D. and Clement, M. V.
1115 OpenComet: An automated tool for comet assay image analysis. *Redox Biology* 2, 457–
1116 465 (2014).
- 1117 64. Bolte, S. and Cordelières, F. P. A guided tour into subcellular colocalization
1118 analysis in light microscopy. *Journal of Microscopy* 224, 213–232 (2006).

Global MS/MS Epigenetic Analysis of DNA Damage Response

- 1119 65. Ovesný, M., Křížek, P., Borkovec, J., Švindrych, Z. and Hagen, G. M.
1120 ThunderSTORM: a comprehensive ImageJ plug-in for PALM and STORM data analysis
1121 and super-resolution imaging. *Bioinformatics* 30, 2389–2390 (2014).
- 1122 66. Kim, J. J., Lee, S. Y., and Miller, K. M. Preserving genome integrity and function:
1123 the DNA damage response and histone modifications. *Critical Reviews in Biochemistry*
1124 and *Molecular Biology* 54, 208–241 (2019).
- 1125 67. Polo, S. E. and Jackson, S. P. Dynamics of DNA damage response proteins at
1126 DNA breaks: A focus on protein modifications. *Genes and Development* 25, 409–433
1127 (2011).
- 1128 68. von Stechow, L. and Olsen, J. V. Proteomics insights into DNA damage
1129 response and translating this knowledge to clinical strategies. *Proteomics* 17, 1600018
1130 (2017).
- 1131 69. Arnaudo, A. M. and Garcia, B. A. Proteomic characterization of novel histone
1132 post-translational modifications. *Epigenetics and Chromatin* 6, 1–7 (2013).
- 1133 70. Huang, H., Lin, S., Garcia, B. A. and Zhao, Y. Quantitative proteomic analysis of
1134 histone modifications. *Chemical Reviews* 115, 2376–2418 (2015).
- 1135 71. Sudprasert, W., Navasumrit, P. and Ruchirawat, M. Effects of low-dose gamma
1136 radiation on DNA damage, chromosomal aberration and expression of repair genes in
1137 human blood cells. *International Journal of Hygiene and Environmental Health* 209,
1138 503–511 (2006).
- 1139 72. Banáth, J. P., MacPhail, S. H. and Olive, P. L. Radiation sensitivity, H2AX
1140 phosphorylation, and kinetics of repair of DNA strand breaks in irradiated cervical
1141 cancer cell lines. *Cancer Research* 64, 7144–7149 (2004).

Global MS/MS Epigenetic Analysis of DNA Damage Response

- 1142 73. Dhar, S., Gursoy-yuzugullu, O., Parasuram, R., and Price, B. D. The tale of a tail:
1143 histone H4 acetylation and the repair of DNA breaks. *Philosophical Transactions of the*
1144 *Royal Society B: Biological Sciences* 372, 20160284 (2017).
- 1145 74. Nguyen, A. T. and Zhang, Y. The diverse functions of Dot1 and H3K79
1146 methylation. *Genes and development* 25, 1345–58 (2011).
- 1147 75. Goldberg, A. D., Banaszynski, L. A., Noh, K. M., Lewis, P. W., Elsaesser, S. J.,
1148 Stadler, S., Dewell, S., Law, M., Guo, X., Li, X. and Wen, D. Distinct Factors Control
1149 Histone Variant H3.3 Localization at Specific Genomic Regions. *Cell* 140, 678–691
1150 (2010).
- 1151 76. Boros, J., Arnoult, N., Stroobant, V., Collet, J. F. and Decottignies, A. Polycomb
1152 repressive complex 2 and H3K27me3 cooperate with H3K9 methylation to maintain
1153 heterochromatin protein 1 α at chromatin. *Molecular and cellular biology* 34, 3662–74
1154 (2014).
- 1155 77. Wiles, E. T. and Selker, E. U. H3K27 methylation: a promiscuous repressive
1156 chromatin mark. *Current Opinion in Genetics and Development* 43, 31–37 (2017).
- 1157 78. Izhar, L., Adamson, B., Ciccia, A., Lewis, J., Pontano-Vaites, L., Leng, Y., Liang,
1158 A.C., Westbrook, T.F., Harper, J.W. and Elledge, S.J. A Systematic Analysis of Factors
1159 Localized to Damaged Chromatin Reveals PARP-Dependent Recruitment of
1160 Transcription Factors. *CellReports* 11, 1486–1500 (2015).
- 1161 79. Nichol, J. N., Dup  r  -Richer, D., Ezponda, T., Licht, J. D. and Miller, W. H.
1162 H3K27 Methylation: A Focal Point of Epigenetic Deregulation in Cancer. *Advances in*
1163 *Cancer Research* 131, 59–95 (2016).

Global MS/MS Epigenetic Analysis of DNA Damage Response

- 1164 80. Agger, K., Cloos, P. A., Christensen, J., Pasini, D., Rose, S., Rappsilber, J.,
1165 Issaeva, I., Canaani, E., Salcini, A.E. and Helin, K. UTX and JMJD3 are histone H3K27
1166 demethylases involved in HOX gene regulation and development. *Nature* 449, 731–734
1167 (2007).
- 1168 81. Murai, J., Shar-yin, N. H., Das, B. B., Renaud, A., Zhang, Y., Doroshov, J. H., Ji,
1169 J., Takeda, S. and Pommier, Y. Trapping of PARP1 and PARP2 by clinical PARP
1170 inhibitors. *Cancer Research* 72, 5588–5599 (2012).
- 1171 82. Sollier, J. and Cimprich, K. A. Breaking bad: R-loops and genome integrity.
1172 *Trends in Cell Biology* 25, 514–522 (2015).
- 1173 83. Aguilera, A. and Gómez-González, B. DNA-RNA hybrids: The risks of DNA
1174 breakage during transcription. *Nature Structural and Molecular Biology* 24, 439–443
1175 (2017).
- 1176 84. Feringa, F. M., Raaijmakers, J. A., Hadders, M. A., Vaarting, C., Macurek, L.,
1177 Heitink, L., Krenning, L. and Medema, R. H. Persistent repair intermediates induce
1178 senescence. *Nature Communications* 9, 3923 (2018).
- 1179 85. Labay, E., Efimova, E. V., Quarshie, B. K., Golden, D. W., Weichselbaum, R. R.
1180 and Kron, S. J. Ionizing radiation-induced foci persistence screen to discover enhancers
1181 of accelerated senescence. *International journal of high throughput screening* 2, 1
1182 (2011).
- 1183 86. Fumagalli, M., Rossiello, F., Mondello, C. and D’Adda Di Fagagna, F. Stable
1184 cellular senescence is associated with persistent DDR activation. *PLoS ONE* 9, 44–46
1185 (2014).

Global MS/MS Epigenetic Analysis of DNA Damage Response

- 1186 87. Liu, Y., Efimova, E. V., Ramamurthy, A. and Kron, S. J. Repair-independent
1187 functions of DNA-PKcs protect irradiated cells from mitotic slippage and accelerated
1188 senescence. *Journal of Cell Science* 132, 13 (2019).
- 1189 88. Fumagalli, M., Rossiello, F., Clerici, M., Barozzi, S., Cittaro, D., Kaplunov, J. M.,
1190 Bucci, G., Dobрева, M., Matti, V., Beausejour, C. M. and Herbig, U. Telomeric DNA
1191 damage is irreparable and causes persistent DNA-damage-response activation. *Nature*
1192 *Cell Biology* 14, 355–365 (2012).
- 1193 89. Ogiwara, H., Ui, A., Otsuka, A., Satoh, H., Yokomi, I., Nakajima, S., Yasui, A.,
1194 Yokota, J. and Kohno, T. Histone acetylation by CBP and p300 at double-strand break
1195 sites facilitates SWI/SNF chromatin remodeling and the recruitment of non-homologous
1196 end joining factors. *Oncogene* 30, 2135–2146 (2011).
- 1197 90. Kruhlak, M. J., Celeste, A., Dellaire, G., Fernandez-Capetillo, O., Müller, W. G.,
1198 McNally, J. G., Bazett-Jones, D. P. and Nussenzweig, A. Changes in chromatin
1199 structure and mobility in living cells at sites of DNA double-strand breaks. *The Journal of*
1200 *Cell Biology* 172, 823-34 (2006)
- 1201 91. Ziv, Y., Bielopolski, D., Galanty, Y., Lukas, C., Taya, Y., Schultz, D. C., Lukas, J.,
1202 Bekker-Jensen, S., Bartek, J. and Shiloh, Y. Chromatin relaxation in response to DNA
1203 double-strand breaks is modulated by a novel ATM-and KAP-1 dependent pathway.
1204 *Nature Cell Biology* 8, 870–876 (2006).
- 1205 92. Sellou, H., Lebeaupin, T., Chapuis, C., Smith, R., Hegele, A., Singh, H. R.,
1206 Kozlowski, M., Bultmann, S., Ladurner, A. G., Timinszky, G. and Huet, S. The
1207 poly(ADP-ribose)-dependent chromatin remodeler Alc1 induces local chromatin
1208 relaxation upon DNA damage. *Molecular Biology of the Cell* 27, 3791–3799 (2016).

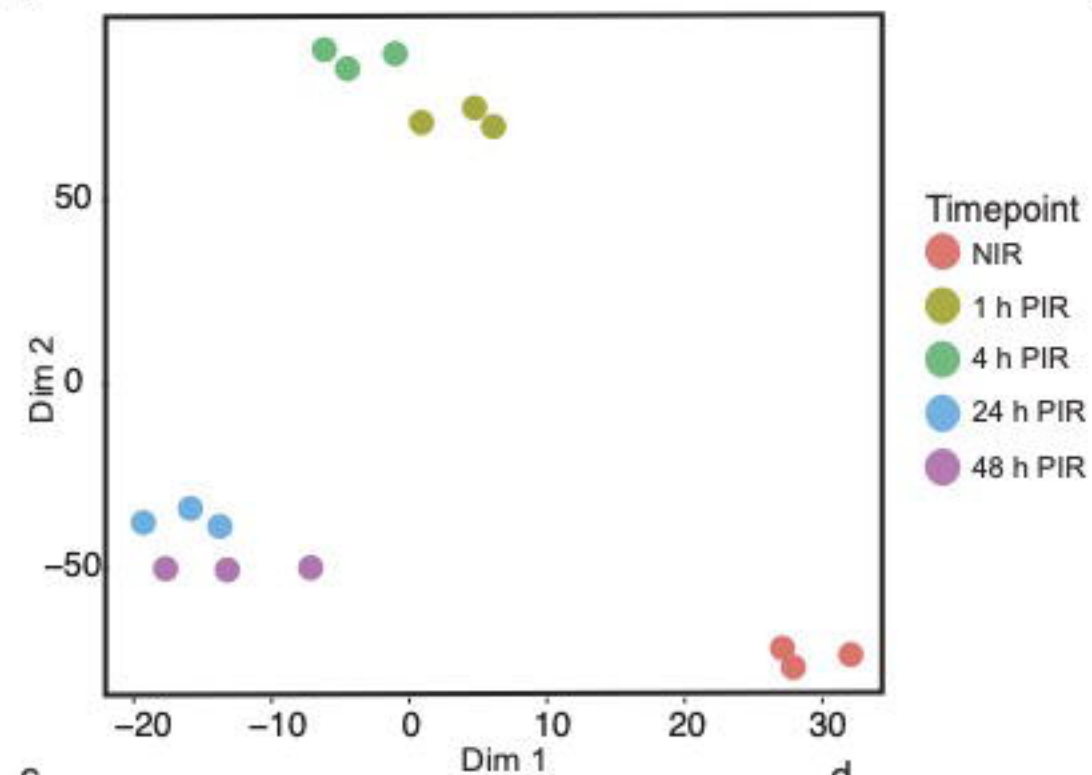
Global MS/MS Epigenetic Analysis of DNA Damage Response

- 1209 93. Barone, F., Belli, M., Pazzaglia, S., Sapora, O. and Tabocchini, M. A. Radiation
1210 damage and chromatin structure. *Annali dell'Istituto superiore di sanita* 25, 59—67
1211 (1989).
- 1212 94. Vissers, J. H. A., van Lohuizen, M. and Citterio, E. The emerging role of
1213 Polycomb repressors in the response to DNA damage. *Journal of Cell Science* 125,
1214 3939–3948 (2012).
- 1215 95. Gong, F., Chiu, L. Y., Cox, B., Aymard, F., Clouaire, T., Leung, J. W.,
1216 Cammarata, M., Perez, M., Agarwal, P., Brodbelt, J. S. and Legube, G. Screen
1217 identifies bromodomain protein ZMYND8 in chromatin recognition of transcription-
1218 associated DNA damage that promotes homologous recombination. *Genes and*
1219 *Development* 29, 197–211 (2015).
- 1220 96. Ito, T., Teo, Y. V., Evans, S. A., Neretti, N. and Sedivy, J. M. Regulation of
1221 Cellular Senescence by Polycomb Chromatin Modifiers through Distinct DNA Damage-
1222 and Histone Methylation-Dependent Pathways. *Cell Reports* 22, 3480–3492 (2018).
- 1223 97. Rath, B. H., Waung, I., Camphausen, K. and Tofilon, P. J. Inhibition of the
1224 histone h3k27 demethylase utx enhances tumor cell radiosensitivity. *Molecular Cancer*
1225 *Therapeutics* 17, 1070–1078 (2018).
- 1226 98. Webb, C. J., Wu, Y. and Zakian, V. A. DNA repair at telomeres: keeping the ends
1227 intact. *Cold Spring Harbor perspectives in biology* 5, (2013).
- 1228 99. Margueron, R. and Reinberg, D. The Polycomb complex PRC2 and its mark in
1229 life. *Nature* 469, 343–349 (2011).
- 1230 100. Lewis, E. B. A gene complex controlling segmentation in *Drosophila*. *Nature* 276,
1231 565–570 (1978).

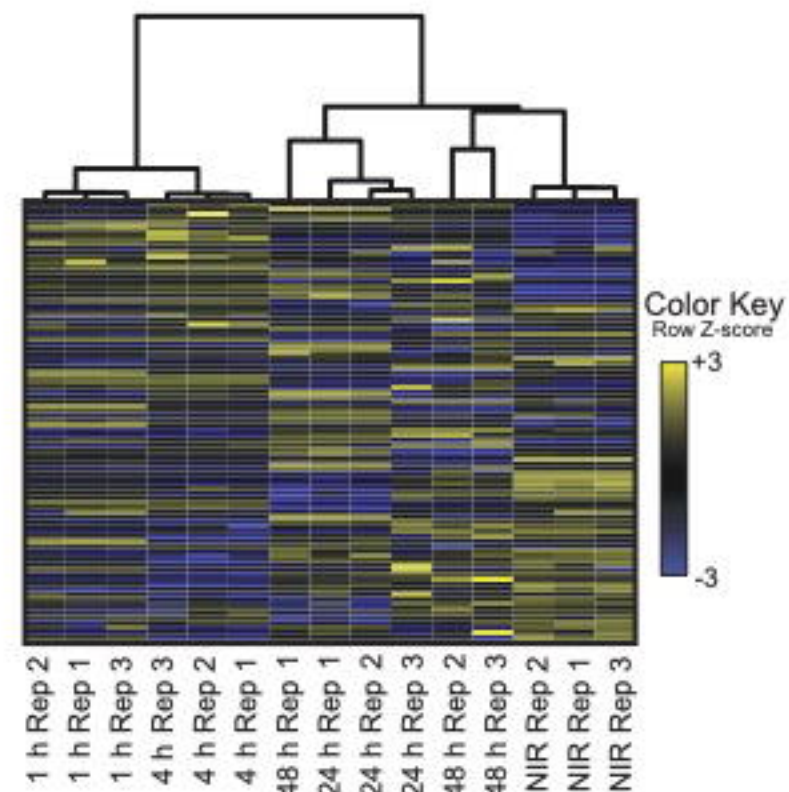
Global MS/MS Epigenetic Analysis of DNA Damage Response

- 1232 101. Marnef, A., Cohen, S. and Legube, G. Transcription-Coupled DNA Double-
1233 Strand Break Repair: Active Genes Need Special Care. *Journal of Molecular Biology*
1234 429, 1277–1288 (2017).
- 1235 102. Gregersen, L. H. and Svejstrup, J. Q. The Cellular Response to Transcription-
1236 Blocking DNA Damage. *Trends in Biochemical Sciences* 43, 327–341 (2018).
- 1237

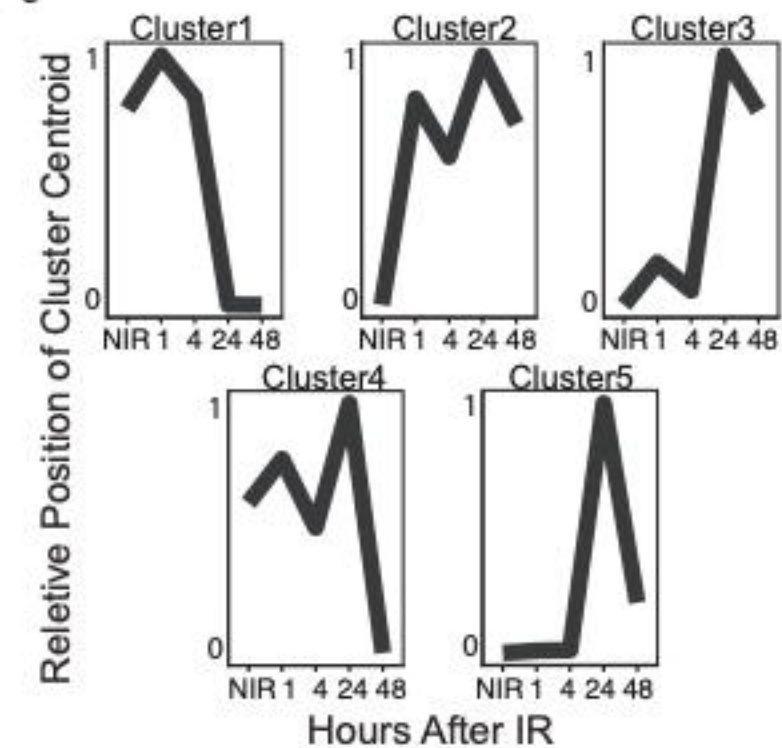
a



b



c



d

